Title

ONC201 in combination with paxalisib for the treatment of H3K27-altered diffuse midline glioma.

Journal

The Journal of cancer research, 83(14)

Authors

Jackson, Evangeline
Duchatel, Ryan
Staudt, Dilana
et al.

Publication Date

2023-05-05

DOI

10.1158/0008-5472.CAN-23-0186

ONC201 in Combination with Paxalisib for the Treatment of H3K27-Altered Diffuse Midline Glioma

Evangeline R. Jackson[1,2], Ryan J. Duchatel[1,2], Dilana E. Staudt[1,2], Mika L. Persson[1,2], Abdul Mannan[1,2], Sridevi Yadavilli[3,4], Sarah Parackal[5,6], Shaye Game[5,6], Wai Chin Chong[5,6], W. Samantha N. Jayasekara[5,6], Marion Le Grand[7], Padraic S. Kearney[1,2], Alicia M. Douglas[1,2], Izac J. Findlay[1,2], Zacary P. Germon[1,2], Holly P. McEwen[1,2], Tyrone S. Beitaki[1,2], Adjanie Patabendige[8,9], David A. Skerrett-Byrne[10,11], Brett Nixon[10,11], Nathan D. Smith[12], Bryan Day[13], Neevika Manoharan[14], Sumanth Nagabushan[14], Jordan R. Hansford[15], Dinisha Govender[16], Geoff B. McCowage[16], Ron Firestein[5,6], Meegan Howlett[17], Raelene Endersby[17], Nicholas G. Gottardo[17,18], Frank Alvaro[2,19], Sebastian M. Waszak[20,21], Martin R. Larsen[22], Yolanda Colino-Sanguino[23,24], Fatima Valdes-Mora[23,24], Andria Rakotomalala[25,26], Samuel Meignan[25,26], Eddy Pasquier[7,27], Nicolas André[7,27,28], Esther Hulleman[29], David D. Eisenstat[30,31], Nicholas A. Vitanza[32,33], Javad Nazarian[3,34,35], Carl Koschmann[36], Sabine Mueller[34,37], Jason E. Cain[5,6], and Matthew D. Dun[1,2,38]

ABSTRACT

Diffuse midline gliomas (DMG), including diffuse intrinsic pontine gliomas (DIPG), are the most lethal of childhood cancers. Palliative radiotherapy is the only established treatment, with median patient survival of 9 to 11 months. ONC201 is a DRD2 antagonist and ClpP agonist that has shown preclinical and emerging clinical efficacy in DMG. However, further work is needed to identify the mechanisms of response of DIPGs to ONC201 treatment and to determine whether recurring genomic features influence response. Using a systems-biological approach, we showed that ONC201 elicits potent agonism of the mitochondrial protease ClpP to drive proteolysis of electron transport chain and tricarboxylic acid cycle proteins. DIPGs harboring *PIK3CA* mutations showed increased sensitivity to ONC201, whereas those harboring *TP53* mutations were more resistant. Metabolic adaptation and reduced sensitivity to ONC201 was promoted by redox-activated PI3K/Akt signaling, which could be counteracted using the brain penetrant PI3K/Akt inhibitor, paxalisib. Together, these discoveries coupled with the powerful anti-DIPG/DMG pharmacokinetic and pharmacodynamic properties of ONC201 and paxalisib have provided the rationale for the ongoing DIPG/DMG phase II combination clinical trial NCT05009992.

Significance: PI3K/Akt signaling promotes metabolic adaptation to ONC201-mediated disruption of mitochondrial energy homeostasis in diffuse intrinsic pontine glioma, highlighting the utility of a combination treatment strategy using ONC201 and the PI3K/Akt inhibitor paxalisib.

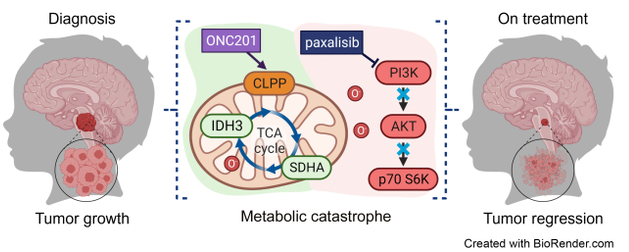

[1]Cancer Signalling Research Group, School of Biomedical Sciences and Pharmacy, College of Health, Medicine and Wellbeing, University of Newcastle, Callaghan, New South Wales, Australia. [2]Precision Medicine Research Program, Hunter Medical Research Institute, New Lambton Heights, New South Wales, Australia. [3]Center for Genetic Medicine Research, Children's National Hospital, Washington, DC. [4]Brain Tumor Institute, Children's National Hospital, Washington, DC. [5]Centre for Cancer Research, Hudson Institute of Medical Research, Clayton, Victoria, Australia. [6]Department of Molecular and Translational Science, Monash University, Clayton, Victoria, Australia. [7]Centre de Recherche en Cancérologie de Marseille, Aix-Marseille Université, Inserm, CNRS, Institut Paoli Calmettes, Marseille, France. [8]Brain Barriers Group, School of Biomedical Sciences and Pharmacy, College of Health, Medicine and Wellbeing, University of Newcastle, Callaghan, New South Wales, Australia. [9]Department of Biology, Edge Hill University, Ormskirk, United Kingdom. [10]School of Environmental and Life Sciences, College of Engineering, Science and Environment, University of Newcastle, Callaghan, New South Wales, Australia. [11]Infertility and Reproduction Research Program, Hunter Medical Research Institute, New Lambton Heights, New South Wales, Australia. [12]Analytical and Biomolecular Research Facility Advanced Mass Spectrometry Unit, University of Newcastle, Callaghan, New South Wales, Australia. [13]QIMR Berghofer Medical Research Institute, Herston, Queensland, Australia. [14]Department of Paediatric Oncology, Sydney Children's Hospital, Randwick, New South Wales, Australia. [15]Michael Rice Cancer Centre, Women's and Children's Hospital, South Australia Health and Medical Research Institute, South Australia ImmunoGenomics Cancer Institute, University of Adelaide, Adelaide, Australia. [16]Department of Oncology, The Children's Hospital at Westmead, Westmead, New South Wales, Australia. [17]Brain Tumor Research Program, Telethon Kids Cancer Centre, Telethon Kids Institute, University of Western Australia, Perth, Australia. [18]Department of Pediatric and Adolescent Oncology and Hematology, Perth Children's Hospital, Perth, Australia. [19]John Hunter Children's Hospital, New Lambton Heights, New South Wales, Australia. [20]Centre for Molecular Medicine Norway (NCMM), Nordic EMBL Partnership, University of Oslo and Oslo University Hospital, Oslo, Norway. [21]Department of Neurology, University of California, San Francisco, San Francisco, California. [22]Department of Biochemistry and Molecular Biology, University of Southern Denmark, Odense M, Denmark. [23]Cancer Epigenetics Biology and Therapeutics, Precision Medicine Theme, Children's Cancer Institute, Sydney, New South Wales, Australia. [24]School of Women's and Children's Health, University of NSW, Sydney, New South Wales, Australia. [25]Tumorigenesis and Resistance to Treatment Unit, Centre Oscar Lambret, Lille, France. [26]University of Lille, CNRS, Inserm, CHU Lille, UMR9020-U1277, CANTHER, Cancer Heterogeneity Plasticity and Resistance to Therapies, Lille, France. [27]Metronomics Global Health Initiative, Marseille, France. [28]Department

Introduction

High-grade gliomas (HGG) are responsible for 10%–15% of all pediatric central nervous system (CNS) cancers, but account for over 40% of deaths (1). Diffuse midline gliomas (DMG), including those of the brainstem (diffuse intrinsic pontine glioma, DIPG) are universally fatal childhood malignancies and responsible for half of all pediatric HGG diagnoses (2). Despite half a century of clinical trials, radiotherapy (RT) remains the only life prolonging treatment for DIPG, with the median overall survival (OS) remaining stagnant at 9–11 months after diagnosis, and <10% of patients with pontine tumors surviving more than 2 years after diagnosis (3, 4). The diffuse and infiltrative growth characteristics of DIPG that enmesh the critical structures of the brainstem make surgical resection extremely challenging. However, over the last 10 years image-guided stereotactic biopsy at diagnosis has been shown to be safe and feasible (5), helping to isolate tumor tissue to identify the recurring molecular (6) and immunological (7) features of the disease.

Global loss of trimethylation at lysine 27 (K27) of histone H3 drives epigenetic dysregulation in primitive neuronal stem cells/oligodendrocyte precursor cells, caused by a methionine to lysine substitution (H3K27M) in either *HIST1H3B* (H3.1) or *H3F3A* (H3.3) genes (8–10) or through the overexpression of *EZHIP* (EZH inhibitory protein) in patients harboring wild-type H3 (11). These H3-alterations inhibit the catalysis of H3K27 trimethylation by the polycomb-repressive complex 2 (12) and co-occur with mutations in tumor suppressor and signaling genes (13). Together, these changes promote the activity of oncogenic signaling cascades that sustain mitogenesis, immune system avoidance, and drive cellular immortality (14).

Preliminary clinical efficacy for the oral, small-molecule imipridone anticancer therapy, ONC201, has been reported in patients diagnosed with DIPG (15) and recurrent H3K27M DMG (16). Previous studies in hematological (17), colorectal (18), breast (19), uterine (20), and non-midline brain cancers (such as glioblastoma; ref. 21), showed ONC201-triggered p53-independent cancer cell apoptosis driven in part by an atypical integrated stress response, initiating expression of the antitumor protein TRAIL (22, 23). The identification of a durable objective response observed in a patient with a secondary glioblastoma harboring an H3.3K27M mutation encouraged continued testing in patients with these mutations, such as DIPG (21).

Described as a dopamine receptor D2 (DRD2) selective antagonist, corroborated by Bayesian machine-learning approaches (24), more recent studies show that ONC201 is also a potent agonist of the ATP-dependent Clp protease proteolytic subunit (ClpP), a mitochondrial protein that degrades mitochondrial respiratory chain proteins to disrupt energy homeostasis (23, 25). Recently, mRNA expression analysis correlated *CLPP* expression with tumor grade and OS in DMG (25). These studies also demonstrated that DMG cell lines with sensitivity to ONC201 and ONC206 (a fluorinated analog of ONC201 in a phase I pediatric clinical trial for DMG PNOC023, NCT04732065), impaired tumor cell metabolism and caused mitochondrial damage, inducing reactive oxygen species (ROS) production to activate an integrative stress response and apoptosis *in vitro* and *in vivo*.

Metabolic effects highlight the potential of ONC201 for the treatment of DIPG, potentially circumventing the inter- and intra-tumoral heterogeneity that has previously plagued the use of precision therapy–based approaches (6). Indeed, ONC201 induces a state of energy depletion as outlined by a significant decrease in ATP levels and a hypophosphorylated state in glioblastoma (26). Potentially, ONC201 represents an important first step in the establishment of a recognized targeted treatment strategy for some patients with H3K27-altered DMG; however, monotherapeutic benefits are transient, whereas for other patients, ONC201 offers no survival improvements and these individuals succumb quickly (27).

Here, we use a systems-wide approach to identify combination strategies to increase the therapeutic response to ONC201, thereby providing the preclinical and preliminary clinical evidence for the commencement of the phase II clinical trial to test ONC201 in combination with the potent brain-penetrant PI3K/Akt inhibitor, paxalisib (28, 29), for the treatment of patients with H3K27M DIPG and DMG at diagnosis and disease progression (NCT05009992).

Materials and Methods

Reagents

Unless otherwise stated, all reagents were obtained from Thermo Fisher Scientific.

Drugs

ONC201 (Chimerix) and paxalisib (Kazia Therapeutics Limited) were obtained under a materials transfer agreement.

Cell lines

The use of patient-derived DIPG neurosphere cell cultures in this study was approved by the Human Ethics Research Committee, University of Newcastle (H-2018–0241). Cell lines (summarized in Supplementary Table S1) were cultured as previously described (30).

Sensitivity

Drug effect on cellular growth and proliferation was determined using the resazurin cell proliferation assay as previously established (15). Briefly, DIPG cells were seeded at 2.5×10^4 cells/well in

of Pediatric Oncology, La Timone Children's Hospital, AP-HM, Marseille, France. [29]Princess Máxima Center for Pediatric Oncology, Utrecht, the Netherlands. [30]Children's Cancer Centre, The Royal Children's Hospital Melbourne, Parkville, Victoria, Australia. [31]Neuro-Oncology Laboratory, Murdoch Children's Research Institute, Department of Paediatrics, University of Melbourne, Parkville, Victoria, Australia. [32]Ben Towne Center for Childhood Cancer Research, Seattle Children's Research Institute, Seattle, Washington. [33]Division of Pediatric Hematology/Oncology, Department of Pediatrics, Seattle Children's Hospital, Seattle, Washington. [34]Department of Pediatrics, University Children's Hospital Zurich, Zurich, Switzerland. [35]The George Washington University, School of Medicine and Health Sciences, Washington, DC. [36]Division of Pediatric Hematology/Oncology, Department of Pediatrics, University of Michigan, Ann Arbor, Michigan. [37]Department of Neurology, Neurosurgery and Pediatric, University of California, San Francisco, California. [38]Paediatric Program, Mark Hughes Foundation Centre for Brain Cancer Research, College of Health, Medicine, and Wellbeing, Callaghan, New South Wales, Australia.

E.R. Jackson, R.J. Duchatel, and D.E. Staudt contributed equally as co-first authors of this article.

Corresponding Authors: Matthew D. Dun, The University of Newcastle, Level 3, Life Sciences Building, Callaghan, NSW 2308, Australia. Phone: 612-4921-5693; E-mail: matt.dun@newcastle.edu.au; Sabine Mueller, sabine.mueller@ucsf.edu; Jason E. Cain, jason.cain@hudson.org.au; Carl Koschmann, ckoschma@med.umich.edu; and Javad Nazarian, Javad.Nazarian@kispi.uzh.ch

Cancer Res 2023;83:2421–37

doi: 10.1158/0008-5472.CAN-23-0186

a 96-well plate, incubated overnight at 37°C and treated with a 1:2 serial dilution of ONC201 from 150 μmol/L for 96 hours. Cells were treated as neurospheres without growth matrix. For low-oxygen testing, DIPG cells were grown in 5% O_2 conditions for at least 1 week before commencement of assays. Plates were read using a Fluostar system at 544/590 nm and values graphed compared with the untreated control.

Annexin-V FITC assay

Cell death was measured using an Annexin-V FITC apoptosis detection kit (BD Biosciences) as previously established (15). Cells were seeded at a density of 5×10^4 per well in a 96-well plate and were incubated with ONC201, for 96 hours before propidium iodide and Annexin V staining as per the manufacturer's recommendations. Stained cells were analyzed using a FACS Canto II flow cytometer and data were processed using FlowJo software.

Colony formation assay

SU-DIPG-VI colony forming ability was assessed via soft agar growth matrix colony formation assay as previously described (31). A total of 3,000 SU-DIPG-VI cells/well were plated into the top agar layer of 24-well plates with indicated doses. MTT was used to count proliferative cells after 2 weeks of growth (5% CO_2 conditions). These data were analyzed with ImageJ and are presented as colony number compared with untreated wells, performed in biological triplicate.

Western blotting

Protein was extracted from DIPG cells using RIPA buffer as per the manufacturer's recommendations and previously described (32). BCA quantification was performed using a Pierce BCA Protein Assay Kit (catalog no. 23227) according to the manufacturer's instructions. Primary antibodies were incubated overnight at dilutions described in Supplementary Table S2. Secondary horseradish peroxidase (HRP)–conjugated antibody (1662408; Bio-Rad) was used at a dilution of 1:5,000. Labeled protein bands were imaged using enhanced chemiluminescence (ECL—Classico, Crescendo; Merck KGaA) in combination with a Chemidoc MP Imaging System (Bio-Rad) and data were analyzed using ImageLab software.

Res259 H3 mutation transfection

The human pediatric glioma cell line Res259 (grade II, diffuse astrocytoma) was transfected to express the wild-type or mutated histone H3 forms, using a Cell Line Nucleofector Kit V (Lonza) with 1 μg of the plasmid containing K27M-mutated *H3F3A* or *HIST1H3B* gene fused with the *mCherry* gene, and bearing a resistance gene for Hygromycin B. As a control, cells were transfected with a similar plasmid containing the wild-type *H3F3A* or *HIST1H3B* gene. Cells were selected using Hygromycin B and sorted for mCherry expression. Histones PTMs were collected using a histone extraction kit (Abcam ab113476) and analyzed using immunoblotting.

CRISPR/Cas9

A total of 2×10^5 cells were seeded in a 6-well plate and incubated overnight. Cells were then replenished with fresh complete media containing 5 μg/mL polybrene (Thermo Fisher Scientific). A 250 μL aliquot of lentiviral cocktail containing either Lenti-Cas9-Blast plasmid (SU-DIPG 13; Addgene), Lenti-Cas9–2A-Blast (SU-DIPG 36; Addgene) or FUCas9Cherry (DIPG-HSJD-007; Addgene) was supplemented into the cell media and incubated for 72 hours. Transduced cells were selectively maintained in complete media containing 10 μg/mL blasticidin (Jomar Life Research) for at least 7 days, or sorted for mCherry expression, before experiment. *CLPP, DRD2, TP53*, and nontargeting control (NTC) single guide RNAs (sgRNA), cloned into the U6-gRNA/hPGK-puro-2A-BFP vector, were obtained from the Human Sanger Whole-Genome Lentiviral CRISPR Library (Thermo Fisher Scientific). The details of gRNA sequence for the *CLPP, DRD2*, and *TP53* were as follows: *CLPP*: 5′-GGTGTGGTGACCGCGGGCCTGG-3′, *DRD2*: 5′-GGCAATGATGCACTCGTTCTGG-3′, *TP53*: 5′-CTCGAAGCGCTCACGCCCACGG-3′.

A total of 5×10^5 Lenti-X HEK29T were seeded in 6-well plates and the following day were transfected with sgRNA plasmids along with the viral packaging plasmids, psPAX-D64V (Addgene) and pMD2.G (Addgene) using Lipofectamine LTX Reagent with PLUS reagent as per the manufacturer's recommendations. Transfection media were replaced with fresh media after 6 hours and incubated for a further 72 hours before collection of virus-containing media. Viral media were added to 2×10^5 Cas9-expressing DMG cells in a 6-well plate in the presence of 1 μg/mL polybrene, centrifuged at $800 \times g$ for 30 minutes and then incubated for 72 hours. Selection of transduced cells using 2 μg/mL of puromycin in fresh media was performed until non-transduced control cells were dead. Heterogenous cell lines were maintained in 2 μg/mL puromycin. For the establishment of single-cell clones from the heterogenous population, single BFP–positive cells were sorted in 96-well plates containing a 1:1 mixture of conditioned media and fresh media. Single-cell clones were expanded and screened using immunoblotting to identify clones with reduced or absent target protein.

Mass spectrometry

Proteomic analysis was conducted as previously reported (33). Briefly, protein was extracted from DIPG cells using a Na_2CO_3 solubilization method capable of differentiating between soluble and membrane bound proteins. Oasis solid-phase extraction columns (Waters) were blocked using a trypsin digest of BSA before being used to desalt protein extracts. A total of 100 μg of each sample (as determined by Qubit 2.0 Fluorometer quantification) was labeled with TMT 16 plex pro labeling tags (as per Supplementary Table S3) according to the manufacturer's instructions. Samples were fractionated by offline high-pH reverse phase fractionation using a Dionex Ultra 3000 uHPLC system (Thermo Fisher Scientific) using nano Ease M/Z Peptide CSH C18 column (130 A, 1.7 μm, 300 μm × 100 mm; Waters). LC/MS-MS was performed using EASY-nLC 1000 (Thermo Fisher Scientific) coupled online to an Orbitrap Exploris 480 mass spectrometer (Thermo Fisher Scientific). Raw files were processed via Proteome Discoverer 2.5.

Hierarchical clustering was performed using Perseus. For our parameters, we used a Euclidean distance, with average linkage and no constraint. A pre-process with *k*-means was performed, with a maximum of 300 clusters, no more than 10 iterations and 1 restart. Because of the small size of some clusters, we grouped like clusters where the same treatment had similar expression profiles. Cluster 1 was the combination of two clusters, whereas cluster 3 was the combination of 7 clusters, 4 of which with clusters less than 5 genes. Clusters 2 and 4 are standalone. Hierarchical clustering trees have been highlighted. Ingenuity Pathway Analysis (IPA) software (Qiagen) was used for bioinformatic analysis of proteomic dataset. Canonical pathways, and upstream regulator analyses were generated and assessed on the basis of *P* value and z-scores.

DIPG xenograft modeling

All *in vivo* experiments were conducted in compliance with the approved CNH Institutional Animal Care and Use Committee protocol (#30425), the University of Newcastle Animal Care and Ethics Committee (#A-2019–900) and the University of California San Francisco Institutional Animal Care and Use Committee (IACUC). Five-week-old, male, NOD SCID gamma (NSG) mice were implanted with 100,000 SU-DIPG-VI/Luc and 300,000 HSJD-DIPG-007 tumor cells into the pontine region of the brainstem using coordinates with Lambda as the reference point (Y: 1.5 mm, X: 0.8 mm, Z: 5 mm) at a rate of 1 μL/minute. Mice were allowed to recover for 4 and 3 weeks, respectively, before commencement of treatment.

For SU-DIPG-VI/Luc model, ONC201 and paxalisib were administered by oral gavage at 125 mg/kg (PBS) and 10 mg/kg (0.5% methyl cellulose/0.2% Tween 80), respectively, at a frequency of 1 time/wk and 3 times/wk. Animals were monitored for weight loss (compared with base weight) and clinical signs. Dose holidays were given at 10% weight loss and resumed at 5% weight recovery. Mice were humanely sacrificed when neurological symptoms were observed, or with more than 20% weight loss.

For the HSJD-DIPG-007 xenograft model, ONC201 and paxalisib were administered as above, except paxalisib was given twice daily at 5 mg/kg. Mice were treated for 5 weeks. Mice were sacrificed at endpoints as described above.

For the SF8628 study, five to six week-old, female athymic (homozygous, nu/nu) mice were obtained from Harlan-Envigo Laboratory. For tumor inoculation 500,000 human SF8628 DIPG cells with the luciferase reporter gene were intracranially implanted into the right pons as previously described (34). Briefly, anesthetized animals received 2 μL of cell suspensions into the right pontine area, with injection coordinates 1 mm to the right from the lambda, top of lamboid suture, and 4-mm depth. Treatment initiated at day 14, when bioluminescence indicated log phase growth. Mice were euthanized when tumor burden reached levels determined by IACUC guidelines.

Tumor size was monitored bi-weekly, using an IVIS-Lumina III imaging system (PerkinElmer) for SU-DIPG-VI/Luc. For SF8628, bioluminescence was measuring using an IVIS Lumina imaging station (Caliper Life Sciences; ref. 35). Mice were intraperitonially injected with 150 mg/kg of D-luciferin (Gold Biotechnology) and imaged 10 minutes following D-luciferin injection. BLI signal intensities were quantified using the region of interest feature of Living Image software. BLI signal at each time point was plotted as an average of total flux (photons/s) for all animals in each group.

In SU-DIPG-VI/Luc, following 2 *in vivo* treatments with ONC201, paxalisib or combination, brainstems were resected lysed with RIPA buffer, immunoblotting was then performed as described above. Samples for IHC were collected in the middle of the fourth week of treatment in HSJD-DIPG-007 xenograft model and staining was conducted as previously described for H3K27M, Ki67 and SDHA (15). Images were visualized using ImageScope and pixel intensity was quantified using ImageJ in technical triplicates across three biological replicates.

Patient experience

Written informed consent was obtained from each of the families whose child's data are included in this study. Two children with biopsy/autopsy-confirmed H3K27M, *PIK3CA* or *PIK3R1* mutant DIPG were treated with ONC201 and paxalisib.

DIPG patient at 5-year-old was diagnosed in March, 2021 with H3.1K27M, *PIK3R1*, and *ACVR1* mutations. A biopsy was performed in the two weeks following this diagnosis, with RT started soon after. The combination of ONC201 (15 mg/kg) and paxalisib (27 mg/m^2) was started 3 months following diagnosis and is ongoing.

DIPG patient at 16-year-old was diagnosed with H3.3K27M, *TP53*, and *PIK3CA* mutations on the December 19, 2018, without a biopsy. They began radiotherapy and ONC201 (15 mg/kg) treatment on the January 9, 2019. ONC201 alone began in February, 2019. February, 2020 saw further progression, with ONC201 and panobinostat (45 mg daily three times per week), stopped May 20, 2020, at further progression. Re-irradiation and ONC201 began on May 29. ONC201 and paxalisib (27 mg/m^2) dual compassionate use began on June 22, 2020.

Statistical analysis

GraphPad Prism 9 software was used for statistical analyses. Unless otherwise stated, two sample unpaired Student *t* tests or one-way ANOVA was used to determine significant differences between groups. Where samples sizes were smaller, comparing different biological samples, nonparametric tests, one-way ANOVA, and *t* tests were used. Survival analysis was performed using the log-rank test. Values shown are the mean ±SEM. Significance values, *, $P < 0.05$; **, $P < 0.01$; ***, $P < 0.001$; ****, $P < 0.0001$, are used throughout.

Data availability

Data generated in this study have been included in the article and Supplementary Material. The proteomics data are deposited to ProteomeXchange via the PRIDE with the dataset identifier PXD036245 (36). All other raw data are available upon request from the corresponding author.

Results

Comprehensive drug profiling predicts reduced sensitivity to ONC201 in *TP53*-mutant DIPG

Using 13 patient-derived neurosphere-cell culture models harboring DMG molecular subtypes (H3-wt $n = 2$, H3.1K27M $n = 4$, and H3.3K27M $n = 7$) and immortalized neural cell controls (HCMEC/D3 blood–brain barrier endothelial cells, HMC3 microglial cells and ReN neural progenitor cells), we assessed sensitivity to ONC201 via inhibition of proliferation, induction of apoptosis and cell death. Overall, 43% of DIPG models showed >50% reduction in proliferation following ONC201 exposure (**Fig. 1A**; Supplementary Table S4). However, we identified a subpopulation of DIPG models, including controls, which demonstrated <50% reduction in proliferation, even at very high concentrations of ONC201 (>150 μmol/L) for up to 96 hours (**Fig. 1A**; Supplementary Table S4).

Analysis of cell death markers via annexin V/PI cytotoxicity analysis corroborated proliferation data, showing ONC201 is cytotoxic to SU-DIPG-XXXIII ($P = 0.0043$) and HSJD-DIPG-007 ($P = 0.0018$), with UON-JUMP4 and SU-DIPG-XIII demonstrating decreased sensitivity (**Fig. 1B**), akin to previous studies testing ONC201 in DIPG models (15, 25) and at physiologically relevant doses (5 μmol/L; ref. 37). Neurosphere morphology was assessed following a 6-day ONC201 treatment to account for variations in doubling times (Supplementary Fig. S1) across 11 DIPG cell line models. ONC201-sensitive cells showed reduced cell number and less viability, whereas neurosphere models similarly featured less robust sphere formation accompanied by more nonviable, singular cells (**Fig. 1C**, top; Supplementary Fig. S2). By contrast, models with decreased sensitivity retained cell number and neurosphere morphology and presented with fewer differences in nonviable cells compared with untreated controls (**Fig. 1C**, bottom; Supplementary Fig. S2B).

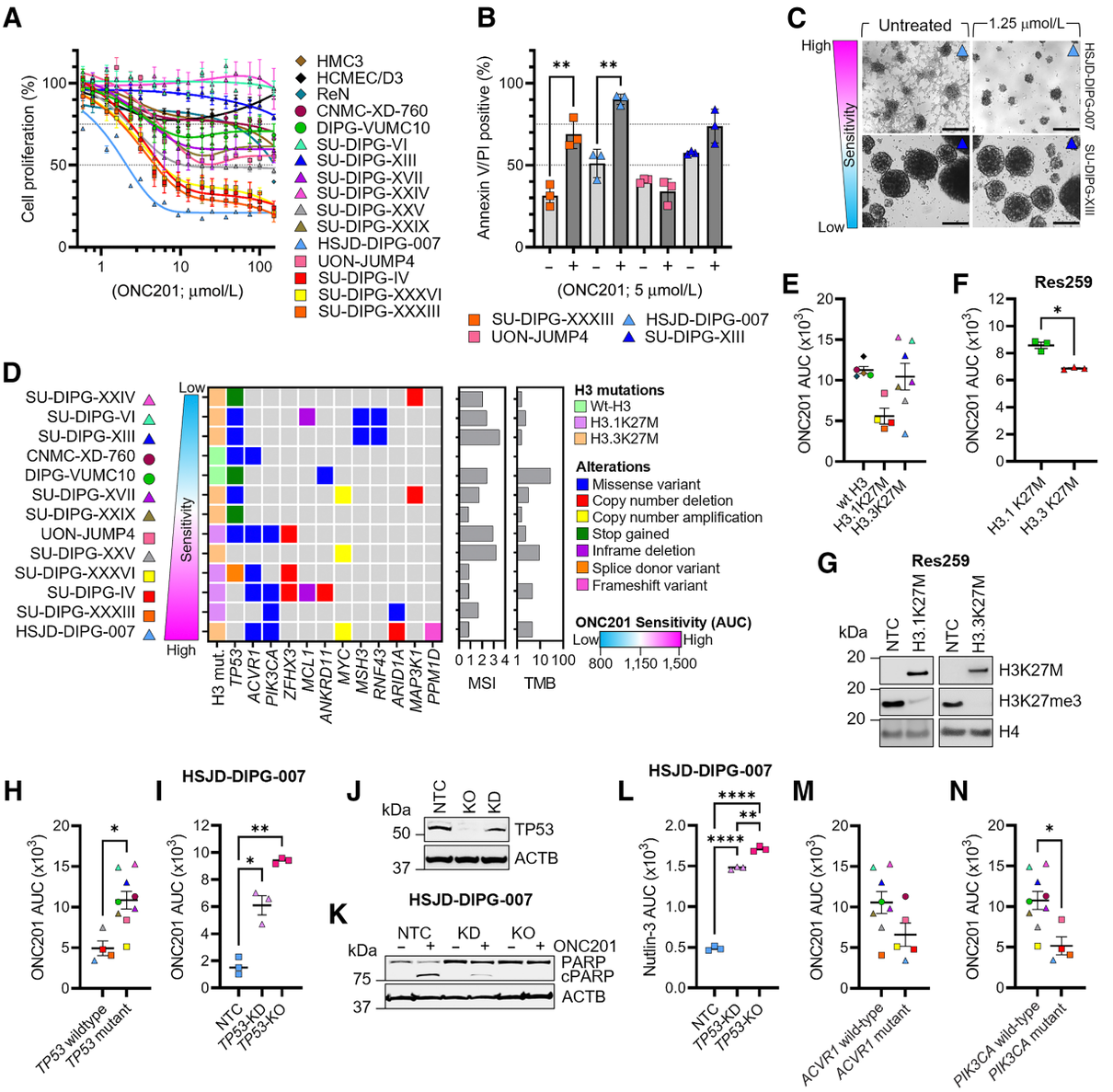

Figure 1.

DIPG patient–derived cell lines show variable response to ONC201 treatment. **A,** Resazurin proliferation (percentage compared with untreated) after 96 hours ONC201 exposure in DIPG patient-derived cell lines; EZHIP+ (circles) = CNMC-XD-760, DIPG-VUMC10; H3.1K27M (squares) = UON-JUMP4, SU-DIPG-IV, SU-DIPG-XXXIII, SU-DIPG-XXXVI, and H3.3K27M (triangles) = HSJD-DIPG-007, SU-DIPG-VI, SU-DIPG-XIII, SU-DIPG-XVII, SU-DIPG-XXIV, SU-DIPG-XXV, SU-DIPG-XXIX. The endothelial cell line, HCMEC/D3, SV-40–dependent human microglial line, HMC3 and neural progenitor cell line, ReN cells, were used as controls (diamonds). Values shown as mean ± SEM ($n = 3$). **B,** Annexin V apoptosis assay after 96 hours exposure with 5 μmol/L ONC201 (dark gray) compared with untreated (light gray) in SU-DIPG-XXXVI, HSJD-DIPG-007, UON-JUMP4, and SU-DIPG-XIII. Unpaired *t* test, values shown as mean ± SEM ($n = 3$). **C,** Representative phase contrast images of biological triplicates ($n = 3$) of HSJD-DIPG-007 and SU-DIPG-XIII following 6 days exposure to 1.25 μmol/L ONC201. Scale bar, 0.2 mm. **D,** Oncoplot of somatic mutations determined using TSO500. Cell lines ordered from the least to most sensitive to ONC201 exposure (top to bottom). Larger values of MSI and TMB are associated with increased pathogenicity. **E,** Proliferation data were grouped by H3 status; wt-H3 ($n = 5$), H3.1K27M ($n = 4$), and H3.3K27M ($n = 7$), and sensitivity to ONC201 was determined by the AUC, ± SEM. Statistical analysis was performed via nonparametric unpaired one-way ANOVA. **F,** Resazurin proliferation, AUC, following ONC201 exposure for 96 hours in Res259 cells harboring knockin of either H3.1K27M or H3.3K27M mutations. Statistical analysis performed via parametric unpaired *t* test, with Welch correction. **G,** Western blot validation of H3K27M knockin in Res259 cells. **H,** *TP53* status, wt- and mutant-*TP53* ($n = 4$ vs. $n = 9$), and sensitivity to ONC201 were determined by the AUC, with values shown as mean ± SEM. Statistical analysis performed via nonparametric unpaired *t* test. **I,** Resazurin proliferation, AUC, following ONC201 exposure in wt-*TP53* HSJD-DIPG-007 DIPG cell lines transduced with a nontargeting control (NTC) gRNA, *TP53*-KD (knockdown), and *TP53*-KO (knockout). Statistical analysis was performed via parametric unpaired one-way ANOVA with Welch correction. **J,** Western Blot confirmation of TP53 KO and KD in HSJD-DIPG-007 cells. **K,** Validation of decreased response to ONC201 in *TP53*-KD or *TP53*-KO HSJD-DIPG-007 cell lines was performed by Western blot analysis of PARP cleavage (cPARP). **L,** Resazurin proliferation, AUC, following Nutlin-3 exposure for 96 hours in HSJD-DIPG-007 NTC, *TP53*-KD, and *TP53*-KO. Statistical analysis was performed via parametric unpaired one-way ANOVA with Welch correction. **M** and **N,** Proliferation data were grouped by ACVR1 status; *ACVR1* wild-type ($n = 8$) versus *ACVR1* mutant ($n = 5$; **M**) and *PIK3CA* status; *PIK3CA* wild-type ($n = 9$) versus *PIK3CA* mutant ($n = 4$; **N**) and compared with AUC following ONC201 exposure. Statistical analysis performed via nonparametric unpaired *t* test. *, $P < 0.05$; **, $P < 0.01$; ****, $P < 0.0001$.

To determine whether recurring mutations influenced the sensitivity of DIPG cell lines to ONC201, we performed pharmacogenomic analysis using next generation sequencing (summarized in **Fig. 1D**). As a means of determining the comparative sensitivity across models, we calculated the AUC of cell lines treated with ONC201 (**Fig. 1A**), and grouped DIPG models by H3K27 status and assessed whether there were differences in sensitivity (**Fig. 1E**). No difference in ONC201 sensitivity was seen in H3K27-altered subtypes (**Fig. 1E**, wt-H3 vs. H3.1K27M, $P = 0.0696$; wt-H3 vs. H3.3K27M, $P = 0.09999$; H3.1K27M vs. H3.3K27M, $P = 0.1711$). In line with previous studies of ONC201 efficacy in glioblastoma models (21), and to confirm the role histone mutations may play in response to ONC201, we knocked in H3.1K27M or H3.3K27M mutations into wt-H3 astrocytoma models (Res259; ref. 38). Res259 cells harbor overexpression of *PDGFRA* and *KIT* (39), which represents a similar genetic architecture to DMGs without the H3/EZHIP alterations. In line with previous studies Res259-H3.3K27M$^+$ cells showed significantly increased sensitivity compared with H3.1K27M$^+$ cells (H3.3K27M vs. H3.1K27M $P = 0.0139$; **Fig. 1F** and **G**; Supplementary Fig. S3A and S3B).

Besides H3K27M alterations, *TP53* loss-of-function mutations (LoF) were the next most frequently identified in our DIPG models ($n = 9$), and included missense variants ($n = 5$), stop gains ($n = 3$) and a splice donor variant ($n = 1$), predominantly affecting H3.3K27M DIPG models (**Fig. 1D**). *TP53*-mutant DIPG models were significantly less sensitive to ONC201 than wt-*TP53* DIPG models ($P = 0.014$; **Fig. 1H**). Receiver operating characteristic (ROC) curve analysis supported the pharmacogenomic observation that *TP53*-mutant DIPGs possessed decreased sensitivity to ONC201 (AUROC = 0.9722, $P = 0.0087$; Supplementary Fig. S3C). To further explore the influence of *TP53* mutations, we performed CRISPR/Cas9-mediated *TP53* knockdown (KD) and single-cell knockout (KO) using the ONC201-sensitive HSJD-DIPG-007 DIPG model, which harbors wt-*TP53*, H3.3K27M and mutant *PPM1D* (**Fig. 1A**, **B**, and **D**). Modulating expression of *TP53* did not influence proliferation rate (Supplementary Fig. S3D); however, in agreement with our pharmacogenomics studies, *TP53* KD/KO decreased sensitivity of HSJD-DIPG-007 to ONC201 treatment compared with nontargeting gRNA controls (ONC201 IC_{50} wt-*TP53* = 2.202 μmol/L, *TP53*-KD = 7.344 μmol/L $P = 0.0117$, *TP53*-KO = NR $P = 0.004$; **Fig. 1I** and **J**; Supplementary Fig. S3E). The role LoF *TP53* mutations in response to ONC201 was further investigated using immunoblotting, which demonstrated that 5 μmol/L ONC201 induced robust cleavage of PARP, indicative of apoptosis in wt-*TP53* cells, moderate cleavage in *TP53*-KD cells, but no cleavage of PARP in *TP53*-KO HSJD-DIPG-007 cells (**Fig. 1K**), corroborating the pharmacogenomic analysis showing that DIPG cells harboring *TP53* mutations show decreased sensitivity to ONC201. Using the small-molecule MDM2 inhibitor of Nutlin-3, we show that KD/KO of *TP53* mimics LoF mutations, driving senescence only in nontransfected control (*TP53*-NTC $IC_{50} = 3.507$; *TP53*-KD and *TP53*-KO IC_{50} = NR) than *TP53*-KD and *TP53*-KO, which did not reach IC_{50} (**Fig. 1L**). Furthermore, even though HSJD-DIPG-007 cells harbor a *PPM1D* mutation, these cells are as sensitive to MDM2 antagonism in line with other *PPM1D* mutant cells lines (40), and conversely to HSJD-DIPG-007 cells harboring *TP53* LoF, show reduced sensitivity to ONC201 (**Fig. 1L**; Supplementary Fig. S3E–S3G). As *TP53* and H3.3K27M mutations are known to associate with aneuploidy, and a chromosomal instability signature, we examined whether *TP53* mutations and ONC201 sensitivity correlated with chromosomal instability (41), through the measurement of tumor mutational burden (TMB), microsatellite instability (MSI; **Fig. 1D**; Supplementary Fig. S3H and S3I) and chromosomal gains and losses (Supplementary Fig. S3J and S3K). No difference between *TP53* status and MSI, TMB or chromosomal gains/losses was observed, suggesting that this may not be a feature of *TP53*-mutant DMGs in our cohort. Furthermore, TSO500 revealed high number of *ACVR1*-mutant DIPGs (38%, $n = 5$), often co-occurring with H3.1K27M (23%, $n = 3$; **Fig. 1D**). We next examined whether *ACVR1* promoted sensitivity to ONC201; however showed no difference in ONC201 sensitivity between wt-*ACRV1* and mutant DIPGs ($P = 0.1274$; **Fig. 1M**). In addition, as *ACVR1* and *PIK3CA* regularly co-occur (23%, $n = 3$), with recurrent *PIK3CA* mutations seen in our DMG models (31%, $n = 4$), we examined whether *PIK3CA* mutations could predict sensitivity and show here that they are more sensitive to ONC201 compared with wt-*PIK3CA* DIPGs ($P = 0.012$; **Fig. 1N**).

Somatic pharmacogenomic analysis identified DRD2 and CLPP to be targets of ONC201 in DIPG

In vitro profiling of the G-protein coupled receptor (GPCR) superfamily has previously shown ONC201 to be a dopamine receptor (DRD2/3/4) antagonist (24), as well as an agonist of the mitochondrial protease ClpP (19, 23). Recently, we performed molecular modeling of both ClpP and DRD2 to show that ONC201 binds to both targets with high affinity (15). Therefore, to identify targets of, and hence pathways influenced by ONC201, we correlated ONC201 sensitivity (z-AUC) with basal gene (Supplementary Fig. S4A) and protein (**Fig. 2A**) expression profiles of known putative targets. High DRD2 protein expression was significantly correlated with increased sensitivity to ONC201 ($R^2 = 0.2348$; $P = 0.0027$; **Fig. 2B**), and at the transcript level ($R^2 = 0.1382$; $P = 0.0431$; Supplementary Fig. S4B). A significant correlation was also identified for ClpP at the protein level ($R^2 = 0.1240$; $P = 0.0352$; **Fig. 2B**); however, not at the transcript level ($R^2 = 0.06571$; $P = 0.1715$; Supplementary Fig. S4B). Pediatric patients with HGG, including patients with DIPG, harbor ubiquitously high-*CLPP* expression, more so than any other pediatric CNS tumor (**Fig. 2C**; ref. 42). Agonism of ClpP by ONC201, increases its proteolytic activity to drive degradation of respiratory chain complex subunits, including Succinate dehydrogenase A and B (SDHA and SDHB), among others (Supplementary Fig. S4C; ref. 23). Succinate dehydrogenase enzymes form integral components of both the TCA cycle and mitochondrial respiratory ETC, and not only oxidize succinate to fumarate to support energy production, but their loss promotes oxidative stress through the production of ROS and release intermediates that control chromatin modifications and gene expression (43). Our recent study of ONC201 used by patients with DIPG, showed that ONC201 elicited potent degradation of SDHA in DIPG patient-derived xenograft (PDX) tumor tissue *in vivo* (15). Analysis shows that SDHA protein expression did nonsignificantly correlate with ONC201 sensitivity ($R^2 = 0.05555$; $P = 0.1664$; **Fig. 2B**), and this was also not at the transcript level ($R^2 = 0.118$; $P = 0.071$; Supplementary Fig. S4B). However, the ratio of SDHA (proteolytic target) to ClpP (protease) protein expression profiles may influence DMG cell sensitivity to ONC201 ($R^2 = 0.1823$; $P = 0.0094$; **Fig. 2B**), providing further evidence that ClpP is a target of ONC201 in DIPG. We further examined the role of ClpP and DRD2 in mediating ONC201 sensitivity using CRISPR/Cas9–mediated KD (**Fig. 2D**). Indeed, loss of *CLPP* expression had no effect on the ONC201-cell line harboring reduced sensitivity (SU-DIPG-XIII) yet abrogated the effects of ONC201 in the sensitive line (SU-DIPG-XXXVI; **Fig. 2D** and **E**). Interestingly, DRD2 was shown to be indispensable for DIPG cell line proliferation *in vitro*, regardless of sensitivity (**Fig. 2D** and **E**), analogous to *in vitro* and *in vivo* studies performed in patient-derived glioblastoma models (44).

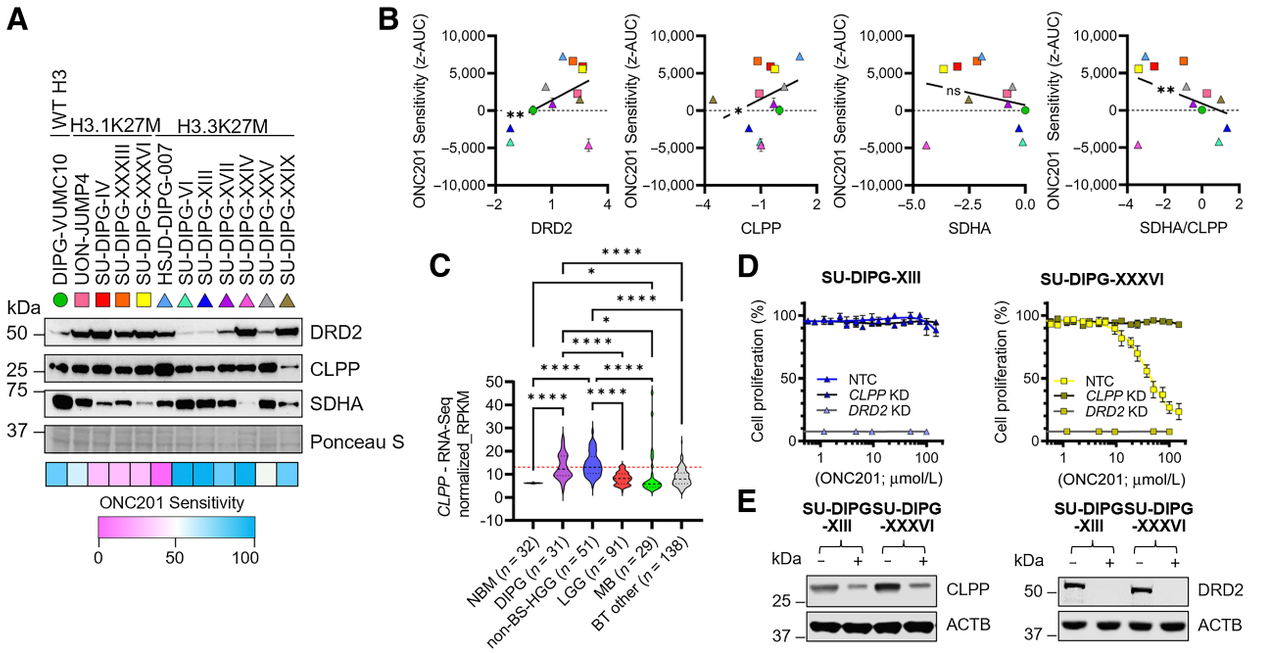

Figure 2.

Pharmacoproteogenomic analysis identifies DRD2 and ClpP as targets of ONC201 in DIPG. **A,** Western blot analysis of basal DRD2, SDHA, and CLPP expression across DIPG models. **B,** Densitometry of protein expressions was normalized to DIPG-VUMC10 and compared with the z-AUC (median AUC) for the control cell lines (HMC3, HCMEC/D3, ReN)—AUC of DIPG cells after exposure to ONC201. Pearson linear regression, accounting for replicates, was used to determine ONC201 sensitivity correlation for DRD2, CLPP, SDHA, and the ratio of SDHA to CLPP (SDHA/CLPP). ns, not significant; $n = 12$. **C,** *CLPP* RNA expression from RNA-seq data publicly available through St Jude's PeCan database, normalized to FPKM (fragments per kilobase of transcript per million mapped reads). NBM (normal bone marrow CD34-positive hemopoietic stem cells/mononuclear cells), DIPG (diffuse intrinsic pontine glioma), non-BS-HGG (non-brainstem-high grade glioma, including not otherwise specified), LGG (low-grade glioma), MB (medulloblastoma), and BT other (brain tumor other—ependymoma, atypical teratoid rhabdoid tumor, choroid plexus carcinoma, cranio and CNS tumor not specified). Statistical significance determined via one-way ANOVA. **D,** Resazurin proliferation following ONC201 exposure (compared with untreated, 96 hours) of CRIPSR-Cas9–mediated knockdown of *CLPP* and *DRD2* was performed in SU-DIPG-XIII (blue) and SU-DIPG-XXXVI (yellow). Values shown as mean ± SEM ($n = 3$). **E,** Western blot validation of successful knockdown of CLPP and DRD2 in SU-DIPG-XIII and SU-DIPG-XXXVI. *, $P < 0.05$; **, $P < 0.01$; ****, $P < 0.0001$.

Quantitative proteomic profiling confirms that ONC201 drives mitochondrial degradation, rescued by redox-regulated PI3K/Akt signaling

Pharmacogenomics coupled with gene editing predicted *TP53* mutations/LoF to influence sensitivity to ONC201 (**Fig. 1**), which is at odds with previous studies in non-DIPG cancers (17, 22). However, biochemical correlation of putative targets, including DRD2 and ClpP, supports previously identified mechanisms of the anticancer effects of ONC201 in non-DIPG cells.

Given the critical role SDHA plays in mitochondrial respiration, we performed high-resolution quantitative proteomic profiling following ONC201 exposure (5 μmol/L, 24 hours) in both normoxic and low-oxygen conditions to mimic the spatial heterogeneity of DIPG using SU-DIPG-VI cells (H3.3K27M, *TP53*-mutant, DRD2-low, SDHA-high, ONC201 resistant; Supplementary Table S5). Hierarchical clustering revealed subtle but significant changes in protein expression induced by ONC201 treatment in cells grown under different oxygen tensions (Supplementary Fig. S5A). By interrogating differentially and commonly expressed clusters, assigned using the differences influenced by ONC201 or oxygen concentration (Supplementary Fig. S5B and S5C) using IPA, we identified mitochondrial dysfunction as the most significantly altered canonical process across these clusters and across both oxygen tensions following ONC201 treatment ($P =$ 1E−27; **Fig. 3A**; Supplementary Fig. S5B–S5D; Supplementary Tables S6–S8), with oxidative phosphorylation the most significantly downregulated cellular process ($P = 1.58e{-}24$, z-score = −4.49; **Fig. 3A**; Supplementary Fig. S5B and S5C). Activated upstream regulator analysis further revealed the role that ONC201 plays in promoting ClpP ($P = 6.65E{-}09$, z-score = 3.051) and KDM5A ($P =$ 2.22E−15, z-score = 4.2) activity, disrupting mitochondrial homeostasis ($P = 6.65E{-}09$, z-score = 3.051; **Fig. 3B**) and degrading mitochondrial and tricarboxylic acid cycle (TCA) proteins (SDHA, $P = 2.58E{-}04$ and IDH3B, $P = 5.29E{-}03$, respectively), as well as additional enzymes of the mitochondrial energy production pathways (**Fig. 3C**). Immunoblotting confirmed the changes in protein expression revealed by mass spectrometry, here ONC201 elicited degradation of mitochondrial proteins SDHA and IDH3A/B and increased phosphorylation of H2AX (**Fig. 3D**).

Protein expression profiles significantly regulated by ONC201 treatment across oxygen tensions predicted the Akt serine/threonine kinase, the key effector of the PI3K pathway, to be upregulated following ONC201 treatment (AKT1, z-score = 2.399; Akt, z-score = 2.349; **Fig. 3B**; Supplementary Table S9). In addition, IL15 activity (z-score = 2.416), which is known to stimulate the JAK–STAT pathway and PI3K/Akt signaling was predicted to be increased (45). Taken together, the predicted increase of PI3K/Akt signaling is potentially responsible for the significantly altered protein expression profiles seen following ONC201 treatment (**Fig. 3E**). These include decreased expression of the proapoptotic protein BAD, increased expression of the antiapoptotic protein BCL2 as well as increased

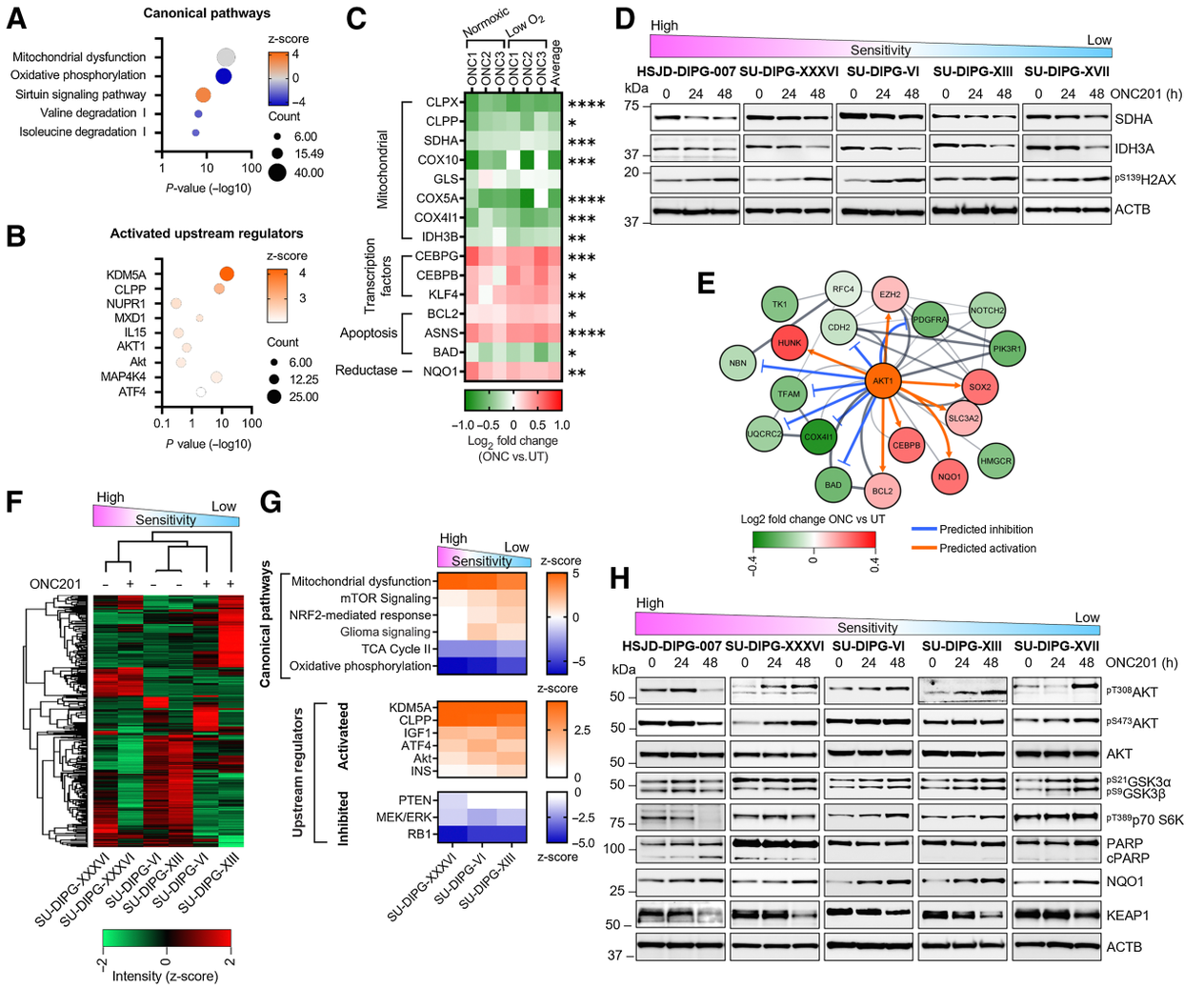

Figure 3.

Quantitative proteomic profiling identifies increased PI3K/Akt signaling in resistant models. High-resolution quantitative proteomic profiling was conducted on SU-DIPG-VI, exposed to 5 μmol/L ONC201 for 24 hours. Cells were treated in low oxygen (5% O_2, 5% CO_2) and normoxic conditions (20% O_2, 5% CO_2) in biological triplicate. **A** and **B,** Major canonical pathways (**A**) and activated upstream regulators (determined by IPA; **B**) of proteins significantly altered following 5 μmol/L ONC201, regardless of oxygen tension (Student *t* test, $P < 0.05$, $n = 6$). **C,** Expression changes of proteins were calculated as $\log_2$-fold change and grouped by mitochondrial proteins, transcription factors, and protein markers of apoptosis. Student *t* test of average change; *, $P < 0.05$; **, $P < 0.01$; ***, $P < 0.001$; ****, $P < 0.0001$. **D,** Orthogonal validation of mitochondrial changes, such as decreased SDHA, was analyzed in DIPG cell lines (HSJD-DIPG-007, SU-DIPG-XXXVI, SU-DIPG-VI, SU-DIPG-XIII, and SU-DIPG-XVII) via Western blot, exposed to 5 μmol/L ONC201 for up to 48 hours. **E,** Network of proteins from upregulated PI3K/Akt signaling predicted by IPA were integrated in Cytoscape StringApp. Predicted increase (orange) and predicted decrease (blue) functional networks indicated with sharp and dark lines linking proteins to indicate a higher confidence interval. Protein expression changes mapped as $\log_2$-fold change of ONC201/untreated calculated using the right-tailed Fisher exact test with the smaller the *P* value, the more likely the association between proteins not to be a random event ($P < 0.05$). **F** and **G,** High-resolution quantitative proteomic profiling was conducted on SU-DIPG-XXXVI, SU-DIPG-VI and SU-DIPG-XXXVI, exposed to 5 μmol/L ONC201 for 24 hours. **F,** Heatmap and unbiased hierarchical clustering of protein expression values normalized using z-score of abundances in Perseus. **G,** Canonical pathways and predicted upstream regulators determined by IPA analysis of proteins altered following ONC201 exposure. Positive z-score value is predictive of pathway activation, whereas a negative z-score is predictive of inhibition. **H,** Orthogonal validation of protein-associated PI3K/Akt/mTOR signaling and the antioxidant-response element (ARE) axis were assessed in DIPG cell lines following ONC201 exposure.

expression of markers of quiescence and progenitor cell types such as SOX2 and EZH2. Predicted increased activity of activating transcription factor 4 (ATF4; z-score = 2.051, $P = 0.0104$; **Fig. 3B**), leading to antiapoptosis through unfolded protein response ($P = 5.89E{-}04$; Supplementary Fig. S5B; ref. 46) is also driven by increased PI3K/Akt signaling, inferring a mechanism of avoiding cell death processes following ONC201 treatment.

To further elucidate the role PI3K/Akt activation may be playing in resistance to ONC201, we performed high-resolution comparative and quantitative proteomic profiling following ONC201 exposure (5 μmol/L, 24 hours) across additional DIPG cell lines with varying sensitivity to ONC201; SU-DIPG-XXXVI, SU-DIPG-XIII and compared with SU-DIPG-VI (**Fig. 3F**). SU-DIPG-VI and SU-DIPG-XIII cells, less sensitive to ONC201 clustered together, away from

SU-DIPG-XXXVI, which is more sensitive to ONC201. Analysis using IPA revealed mitochondrial dysfunction and activation of ClpP/KDM5A following treatment with ONC201 across all cell lines (**Fig. 3G**), further validating ONC201 to be elucidating anti-DIPG effects through mitochondrial dysfunction. Treatment with ONC201 induced activation of PI3K/Akt signaling proteins (**Fig. 3G**), including Akt, IGF1, and downregulated PTEN signaling, in all cell lines, suggesting Akt activation is a reciprocal mechanism associated with ONC201 treatment; however, greater upregulation of Akt signaling was observed in cell lines less sensitive to ONC201 (z-score: Akt SU-DIPG-XXXVI = 1.067, SU-DIPG-VI = 1.692, SU-DIPG-XIII = 2.039, mTOR: SU-DIPG-XXXVI = 0.378, SU-DIPG-VI = 1.134, SU-DIPG-XIII = 1.890). Given that unbiased global proteomic profiling results predicted increased PI3K/Akt activity following ONC201 exposure, we orthogonally validated phosphorylation changes of proteins regulated by this pathway, all of which showed increased phosphorylation in cells refractory to ONC201 following treatment (**Fig. 3H**). Activated PI3K/Akt signaling potentiated phosphorylation of Akt at Thr308 and Ser473 across DIPG lines regardless of ONC201 sensitivity; however, activation of downstream pathway proteins GSK3α, GSK3β, and p70S6K was only present in cell lines showing reduced sensitivity to ONC201 (SU-DIPG-VI, SU-DIPG-XIII, and SU-DIPG-XVII; Supplementary Fig. S5E). In cell lines more sensitive to ONC201, the increase in Akt phosphorylation occurred earlier (24 hours for HSJD-DIPG-007); however, after 48 hours, these cells became apoptotic as indicated by increased cleaved PARP (**Fig. 3H**). Such data align with our recent demonstration that ONC201 drives mitochondrial ROS production and mitochondrial structural abnormalities (25), and thereby links these responses with the oxidative DNA damage seen in these cells (γH2AX, **Fig. 3D**).

Together, the increased mitochondrial oxidative stress caused by ONC201's ClpP agonism and electron leakage (25), commensurate with increased PI3K/Akt signaling activity, may be promoting the activity of the stress sensing transcription factor nuclear factor erythroid 2–related factor 2 (NRF2; **Fig. 3G**), as increased expression of its downstream target, the reductase NQO1 was detected following ONC201 treatment ($\log_2$-fold-change = 0.28, $P = 0.0017$ and orthogonally validated; **Fig. 3C**, **E**, and **H**). NQO1 is responsible for promoting redox homeostasis and cell survival (47). In this regard, KEAP1 is known to regulate the activity of NRF2, and is degraded with ONC201 treatment, leading to decreased abundance (**Fig. 3H**). These observations are in line with previous studies that show loss of expression/degradation of KEAP1 promotes the transcriptional activity of NRF2, resulting in partial epithelial-to-mesenchymal transition but only in tumors harboring *TP53* LoF mutations (48). These observations potentially explain the persistent proliferation of *TP53*-mutant DIPG cells even in the presence of high-dose ONC201.

ONC201-driven oxidative stress drives PI3K/Akt signaling, highlighting the potential of ONC201 combined with the PI3K/Akt inhibitor paxalisib

Proteomic profiling predicted that increased PI3K/Akt signaling may be leading to decreased sensitivity of DIPG cells to ONC201 (**Fig. 3**). Previously, we showed that ONC201 increased ROS production (25); therefore, we used the potent ROS scavenger *N*-acetyl-l-cysteine (NAC) to investigate whether there was a link between increased ROS and increased PI3K/Akt signaling. NAC abrogated phosphorylation of Akt, whereas hydrogen peroxide (H_2O_2) increased phosphorylation (**Fig. 4A**; Supplementary Fig. S6A and S6B). As such, we hypothesized that inhibition of PI3K signaling may prevent the Akt-mediated cell survival signaling induced following exposure to ONC201. To investigate this, we tested whether the brain penetrant PI3K/Akt inhibitor paxalisib (previously GDC-0084; refs. 28, 29) could also suppress PI3K/Akt signaling in response to ONC201. Paxalisib decreased phosphorylation of Akt in the H3.3K27M, *TP53*-mutant and ONC201-refractory model SU-DIPG-XVII either alone or in combination with ONC201 (**Fig. 4B**; ref. 49). Again, ONC201 modulated the abundance of proteins mapping to NRF2-regulated antioxidant response, including the loss of KEAP1, increased NQO1, both abrogated by the combination with paxalisib (**Fig. 4B**) to drive cell death.

To assess adhesion-independent cell proliferation and survival of DIPG cells treated with ONC201, we performed soft agar colony-forming assays using SU-DIPG-VI that show decreased sensitivity to ONC201 as a monotherapy. Encouragingly, at physiologically relevant dosing, single agents decreased colony formation (ONC201 −0.43 $\log_2$-fold, $P = 0.007$; paxalisib −0.5 $\log_2$-fold, $P = 0.0032$), with the combination of ONC201 and paxalisib significantly decreasing colony formation beyond that achieved using either of the single agents (combination vs. UT, −1.4 $\log_2$-fold, $P = <0.0001$, combination vs. ONC201, −1 $\log_2$-fold, $P = 0.0007$, combination vs. paxalisib, −0.93 $\log_2$-fold, $P = 0.0014$; **Fig. 4C**). Indeed, ONC201 in combination with paxalisib synergized, particularly in H3.3K27M *TP53*-mutant DIPG models, regardless of whether the treatment was performed under normoxic or low-oxygen conditions (**Fig. 4D** and **E**; Supplementary Figs. S7, S8A and S8B; Supplementary Table S10); however, the combination was additive in the UON-JUMP4 model, grown in low-oxygen conditions (Supplementary Fig. S8A and S8B). As an additional control, we assessed the sensitivity of human peripheral blood mononuclear cells *in vitro* donated from healthy volunteers to each drug individually and in combination, which revealed no increase in cell death; however, a reduction in PI3K/Akt/mTOR signaling was observed (Supplementary Fig. S8C and S8D).

To determine whether *TP53* status influenced ONC201 PI3K/Akt signaling, we investigated the effect of ONC201 in the *TP53*-KD and *TP53*-KO HSJD-DIPG007 models via immunoblotting. Here, ONC201 decreased SDHA abundance and ERK1/2 phosphorylation regardless of p53 status (**Fig. 4F**). Again, ONC201 significantly increased phosphorylation of Akt at both T308 and S473 residues (**Fig. 4F**; Supplementary Fig. S9) across models, including cells harboring either *TP53*-KD or *TP53*-KO. Interestingly, *TP53*-KD and *TP53*-KO HSJD-DIPG-007 cells harbored significantly increased basal levels of phosphorylation of Akt at T308, a marker of active PI3K signaling compared with the NTCs, which was further potentiated using ONC201 (**Fig. 4F**; Supplementary Fig. S9). Therefore, to determine whether paxalisib could rescue the decreased response promoted by KD and KO of *TP53* in HSJD-DIPG-007 cells, we tested ONC201 in combination with paxalisib and identified very high-level synergy in the *TP53*-KD/*TP53*-KO cells, greater than three times that of parental cells and corresponding to the level of increased PI3K signaling seen (**Fig. 4G** and **H**; Supplementary Fig. S10). Together, these *in vitro* results highlight the potential for the use of paxalisib in combination with ONC201 even in highly aggressive H3.3K27M *TP53*-mutant DIPG models.

Preclinical optimization of ONC201 combined with paxalisib

Clinical trials testing ONC201 and paxalisib as monotherapies in DIPG/DMG have demonstrated acceptable safety and toxicity profiles (NCT03416530 and NCT03696355, respectively). Therefore, to test the preclinical utility of ONC201 combined with paxalisib, we first examined their efficacy using the SU-DIPG-VI/Luc (H3.3K27M, *TP53*-mutant) and HSJD-DIPG-007 (H3.3K27M, *TP53*-wild-type)

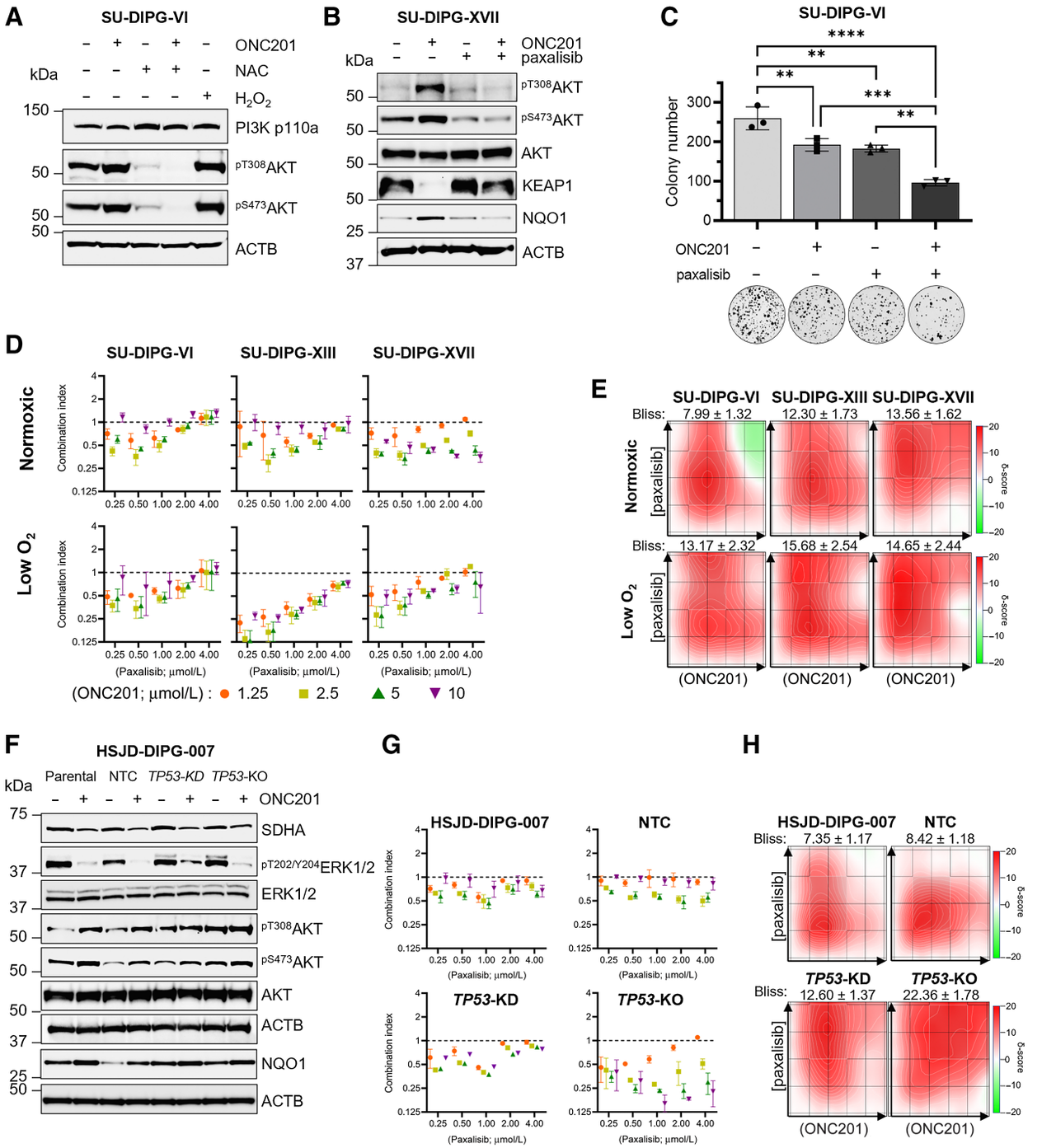

Figure 4.

ONC201 in combination with paxalisib is synergistic across DIPG models. **A,** SU-DIPG-VI was treated with 5 μmol/L ONC201 for 48 hours, 20 mmol/L NAC for 24 hours, and 1 mmol/L H_2O_2 for 1 hour, and protein changes downstream PI3K/Akt and reductase signaling were validated by Western blot. **B,** Western blot analysis of PI3K/Akt, Erk, and antioxidant response element (ARE) signaling in SU-DIPG-XVII treated with 5 μmol/L ONC201 (48 hours) and 1 μmol/L paxalisib (24 hours). **C,** SU-DIPG-VI was grown in soft agarose in colony formation for 2 weeks treated with 0.5 μmol/L ONC201, 100 nmol/L paxalisib, and the combination. The number of colonies was then quantified using ImageJ. Assay was performed in biological triplicate with representative images shown. One-way ANOVA; **, $P < 0.01$; ***, $P < 0.001$; ****, $P < 0.0001$; values shown as mean ± SEM. **D** and **E,** DIPG cells SU-DIPG-VI, SU-DIPG-XIII, and SU-DIPG-XVII were passaged, grown in low oxygen (5% O_2, 5% CO_2) or atmospheric oxygen (20% O_2, 5% CO_2) conditions for a week, and then proliferation assays were performed using ONC201, paxalisib, or both for 96 hours ($n = 3$). Synergy was determined using Chou–Talalay via CompuSyn (**D**) or Bliss synergy (**E**) analysis where a combination index (CI), where <1 (dotted line) demonstrates a synergistic effect and Bliss score >10 represents a strong synergism. **F–H,** Parental wt-*TP53* HSJD-DIPG-007 and HSJD-DIPG-007 cell lines transduced with a nontargeting control (NTC) gRNA, harboring KO or KD of *TP53* were subjected to analysis following ONC201 treatment alone or in combination with paxalisib. **F,** Western blot confirmation of mitochondrial marker, SDHA, PI3K/Akt, Erk, and ARE signaling to ONC201 (5 μmol/L, 48 hours). **G** and **H,** Cells were treated with increasing concentrations of ONC201, paxalisib, or both for 96 hours, in biological triplicate. Synergy was determined using Chou–Talalay (**G**) or Bliss synergy (**H**) analysis. Chou–Talalayand Bliss synergy graphs are reported as mean ± SD.

DIPG xenograft mouse models, using mouse equivalent MTDs (125 mg/kg once a week ONC201, in combination with paxalisib 10 mg/kg three times a week, or 5 mg/kg twice daily, respectively; refs. 42, 43), engrafted into the fourth ventricle/pons of NSG mice (**Fig. 5A**). SU-DIPG-VI/Luc mice were treated continuously and HSJD-DIPG-007 mice were treated for five weeks from treatment start (**Fig. 5A**). *In vivo* bioluminescence imaging (BLI) was performed immediately before drug or vehicle control administration to assess baseline tumor burden (Supplementary Fig. S11A and S11B). Using BLI as a surrogate for tumor size in SU-DIPG-VI/Luc, ONC201 had no significant effect on tumor size, whereas paxalisib significantly reduced tumor burden (paxalisib = 404.84 p sec^{-1} cm^{-2} sr^{-1}, $P = 0.0309$;

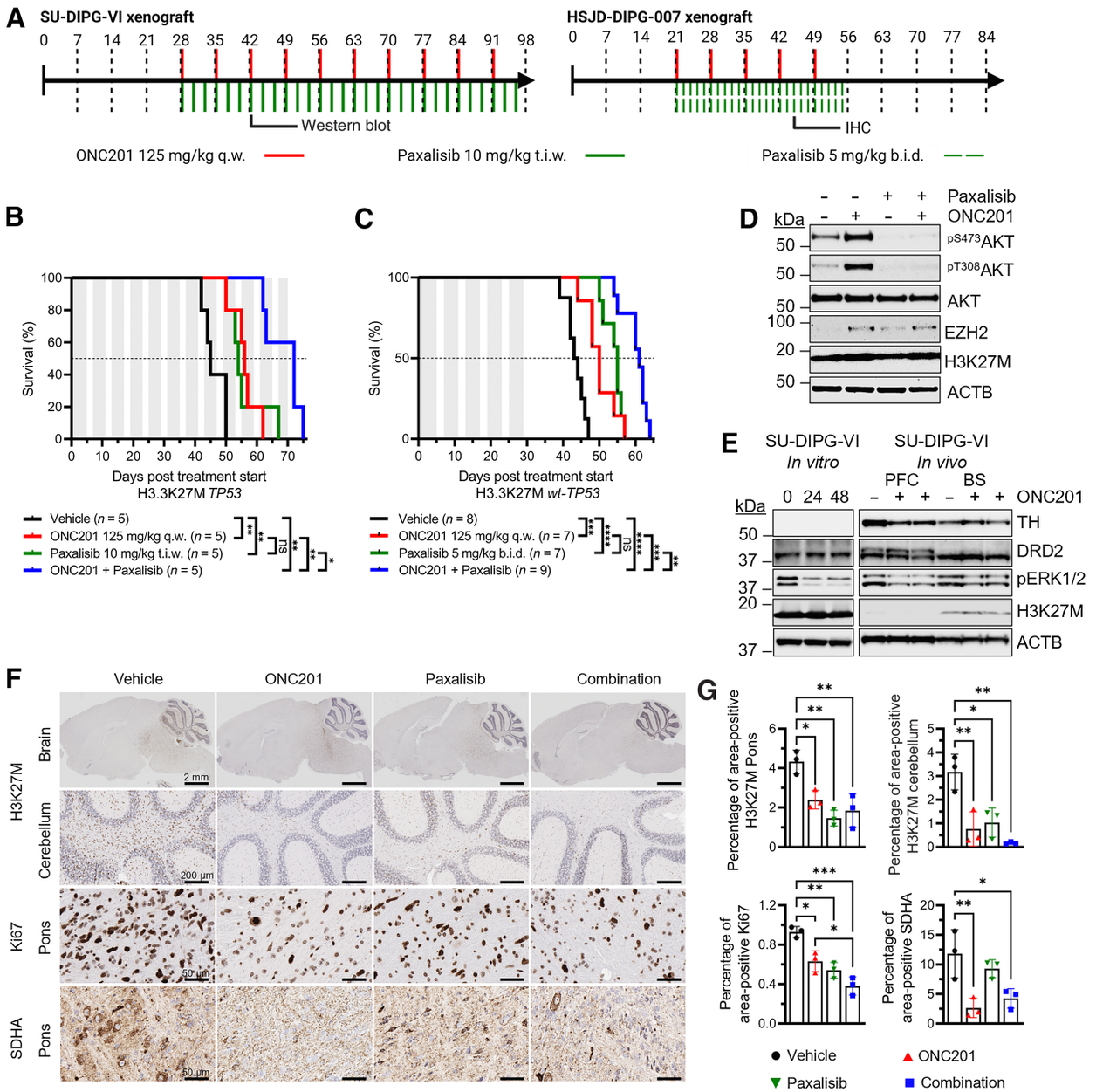

Figure 5.

ONC201 in combination with paxalisib is a synergistic drug combination in DIPG xenograft models. **A,** SU-DIPG-VI/Luc and HSJD-DIPG-007 cells were injected into the brainstem of NSG mice. Treatment was started at 4 or 3 weeks, respectively, from xenograft date. ONC201 and paxalisib were administered by oral gavage. Xenografts were sacrificed for pharmacodynamics and survival was tracked where they were culled at ethical endpoints. **B** and **C,** Survival curve analysis of days after treatment start at animal sacrifice, with significance determined by survival curve comparison for SU-DIPG-VI/Luc (**B**) and HSJD-DIPG-007 (**C**). Shading indicates treatment duration. Log-rank (Mantel–Cox) test. **D,** Tumor tissue from SU-DIPG-VI/Luc xenografts sacrificed at 2 weeks following start of treatment analyzed by Western blot. **E,** SU-DIPG-VI/Luc *in vitro* cells exposed to 5 µmol/L ONC201 for 0, 24, 48, and 72 hours compared with *in vivo* SU-DIPG-VI/Luc tissue collected from the prefrontal cortex (PFC) and brainstem (BS), treated with ONC201. **E,** Tumor tissue was resected from HSJD-DIPG-007 xenografts following 4 weeks of treatment and analyzed by IHC. **F,** Sections were stained for H3K27M, Ki67, and SDHA (representative images are presented). Scale bars, 2 mm, 200 or 50 µm. **G,** IHC images quantified via ImageJ (measured in technical triplicate, across biological replicates, $n = 3$). *, $P < 0.05$; **, $P < 0.01$; ***, $P < 0.001$; ****, $P < 0.0001$; ns, not significant. b.i.d., twice daily; q.w., once a week; t.i.w., three times a week.

Supplementary Fig. S11A and S11B). ONC201, combined with paxalisib, decreased tumor burden throughout the treatment regimen compared with vehicle control (4-week mean BLI ONC201+paxalisib = 158.34 p sec^{-1} cm^{-2} sr^{-1}, $P = 0.0038$).

Both ONC201 and paxalisib as single agents significantly extended the survival of SU-DIPG-VI/Luc xenograft models compared with vehicle controls, with the combination significantly extending the survival compared with all treatments (vehicle = 45 days, ONC201 = 56 $P = 0.0082$, paxalisib = 54 days $P = 0.0082$, ONC201+paxalisib = 72 days, combination vs. vehicle $P = 0.0027$, combination *vs.* paxalisib $P = 0.0198$, and combination *vs.* ONC201 $P = 0.0044$, after treatment start; **Fig. 5B**; ref. 50). In the SU-DIPG/VI model, we identified some early toxicity using 10 mg/kg three times a week (Supplementary Fig. S11C); therefore, treated HSJD-DIPG-007 mice with 5 mg/kg twice daily to improve tolerability (Supplementary Fig. S11D). In the ONC201-sensitive, HSJD-DIPG-007 model, ONC201 provided an increased survival (vehicle = 43.5 vs. ONC201 = 50 days, $P = 0.0009$), and twice daily low-dose paxalisib also provided an improved survival advantage (vehicle vs. paxalisib = 55 days, $P < 0.0001$; **Fig. 5C**). Together the combination both significantly increased survival effect versus controls (combination = 61 days, $P < 0.0001$) and was synergistic compared with monotherapies (ONC201 vs. combination, $P = 0.0003$; paxalisib vs. combination, $P = 0.0019$; **Fig. 5C**). Analogous to *in vitro* studies (**Fig. 4**), tumors resected from SU-DIPG-VI/Luc^+ DIPG xenograft mice treated for two weeks, showed increased Akt phosphorylation and expression of EZH2 following ONC201 treatment alone, consistent with our *in vitro* proteomic profiling, with the former rescued using paxalisib (**Fig. 5D**). To determine the systemic effects of ONC201 treatment *in vivo*, we measured the expression of tyrosine hydroxylase (TH; **Fig. 5E**). ONC201 treatment decreased TH expression in the prefrontal cortex, but not in brainstem where the SU-DIPG-VI cell line was engrafted (**Fig. 5E**). ONC201 decreased Erk phosphorylation in both the prefrontal cortex and brainstem (**Fig. 5E**), commensurate with global effects on DRD2 inhibition, suggesting that systemic effects of DRD2 inhibition and Erk phosphorylation may contribute to efficacy observed in these models. To assess pharmacodynamic markers of treatment response, we performed IHC on fixed tumor tissue following 4 weeks of treatment. Tumor was detected in the pons of all animals; however, compared with the controls, decreased H3K27M staining was seen across biological replicates, including in the cerebellum of treated mice (**Fig. 5F** and **G**; $P < 0.05$). Compared with the controls, decreased staining of the proliferation marker Ki67 was also seen across treatments (ONC201, $P = 0.0114$; paxalisib, $P = 0.0023$; combination $P = 0.0002$), with the combination also significantly decreased compared with ONC201 alone ($P = 0.0275$; **Fig. 5F** and **G**). Significantly decreased staining for SDHA was seen in samples treated with ONC201 and the combination (ONC201, $P = 0.008$; ONC201+paxalisib, $P = 0.0436$, respectively; **Fig. 5F** and **G**).

Using the highly aggressive H3.3K27M SF8628 DIPG xenograft model (51), paxalisib alone and the combination of ONC201 and paxalisib decreased tumor burden at early time points (day 4; vehicle vs. paxalisib, $P = 0.0075$, vehicle vs. combination $P = 0.0152$, day 10; vehicle vs. paxalisib, $P = 0.0042$, vehicle vs. combination $P = 0.0032$; Supplementary Fig. S11E), commensurate with survival analysis, where paxalisib alone provided a significant survival benefit compared with the vehicle (vehicle = 22.5 days, paxalisib = 28 days, $P = 0.0453$) as did the combination therapy (ONC201+paxalisib = 28 days, $P = 0.0002$; Supplementary Fig. S11F). The combination of ONC201 and paxalisib also increased survival of xenograft mice compared with ONC201 alone ($P = 0.0024$), and provided a modest benefit compared with paxalisib alone ($P = 0.0442$; Supplementary Fig. S11F).

Case reports of ONC201 combined with paxalisib in patients with DIPG at diagnosis or disease progression

To demonstrate the potential utility of ONC201 in combination with paxalisib, we report two recent DIPG case studies of patients that received both ONC201 and paxalisib through compassionate access. These patients underwent radiographic analysis according to response assessment in pediatric neuro-oncology (RAPNO). The first is a 6-year-old patient diagnosed in March, 2021, harboring H3.1K27M, *ACVR1*, and *PIK3R1* mutant DIPG identified following biopsy (**Fig. 6A**). At diagnosis, a diffuse pontine lesion was identified (**Fig. 6B** and **C**, tumor area 1,554 mm^2). The patient received 54 Gy of RT delivered in 30 fractions of 1.8 Gy in the 1 to 3 months following diagnosis. After RT MRI indicated a tumor reduction of 38.1% compared with diagnosis (**Fig. 6B** and **D**; tumor area 962 mm^2). The patient began the combination treatment of ONC201 (15 mg/kg once a week) and paxalisib (27 mg/m^2 daily) 7 weeks following the after RT scan, corresponding to 5 months after diagnosis. Tumor size remained relatively stable over the next consecutive MRIs (**Fig. 6E** and **F**, tumor area = 1,156 and 1,224 mm^2, respectively). Encouragingly, 9 months after diagnosis, a substantial 62.1% decrease in tumor area based on T2-weighted images was recorded from the previous MRI, representing a 70.1% reduction compared with diagnosis and 51.8% reduction compared with after RT (**Fig. 6B** and **G**; tumor area = 464 mm^2), showing a partial response. Furthermore, 12 months after diagnosis, 8 months into the ONC201 and paxalisib combination, the tumor had reduced by 80.3% and 68.2%, compared with diagnosis and after RT, respectively (**Fig. 6B** and **H**; tumor area = 306 mm^2). Clinically, 24 months after diagnosis, the tumor remains stable (**Fig. 6I**) and the patient continues to do well, experiencing continued reduction in DIPG-associated clinical symptoms, and has returned to school. Intermittent toxicities during treatment included grade II mucositis during the initial few months on the combination, which responded well to dexamethasone mouthwash.

The second patient with DIPG was a 16-year-old diagnosed with DIPG (tumor area = 977.8 mm^2; **Fig. 6J–L**). The patient did not have a biopsy and began RT in combination with ONC201 (625 mg, once a week) soon after diagnosis. The patient then continued to receive ONC201 as a maintenance therapy. Clinical and radiological signs of first progression were detected 15 months after diagnosis (**Fig. 6K** and **M**; tumor area = 1,303.3 mm^2). The patient then received the combination of ONC201 and panobinostat (45 mg daily three times per week) but stopped after 3 months upon detection of further signs of disease progression (**Fig. 6K** and **N**, tumor area = 1,814 mm^2). The patient then immediately underwent re-irradiation (20 Gy delivered in 10×2 Gy fractions). Paxalisib (45 mg, 27 mg/m^2) was then combined with ONC201 (625 mg) 18 months after diagnosis and continued until the patient succumbed to Pneumocystis pneumonia (PCP), 24 months after diagnosis. The acquired PCP was attributed to concomitant steroid use and hence, the patient was unable to continue either therapy, ultimately passing away 6 months after re-irradiation. T2 axial MR scans during ONC201 and paxalisib treatment showed partial response, with a 34% reduction in total tumor area compared with regression (**Fig. 6N–P**) and 9% reduction during treatment with ONC201 and paxalisib (**Fig. 6O** and **P**), a reduction not seen when ONC201 was combined with RT at diagnosis (**Fig. 6K**, **O**, and **P**). Autopsy analysis revealed viable tumor with no evidence of growth when compared with the latest MRI 1 month earlier, with the family of

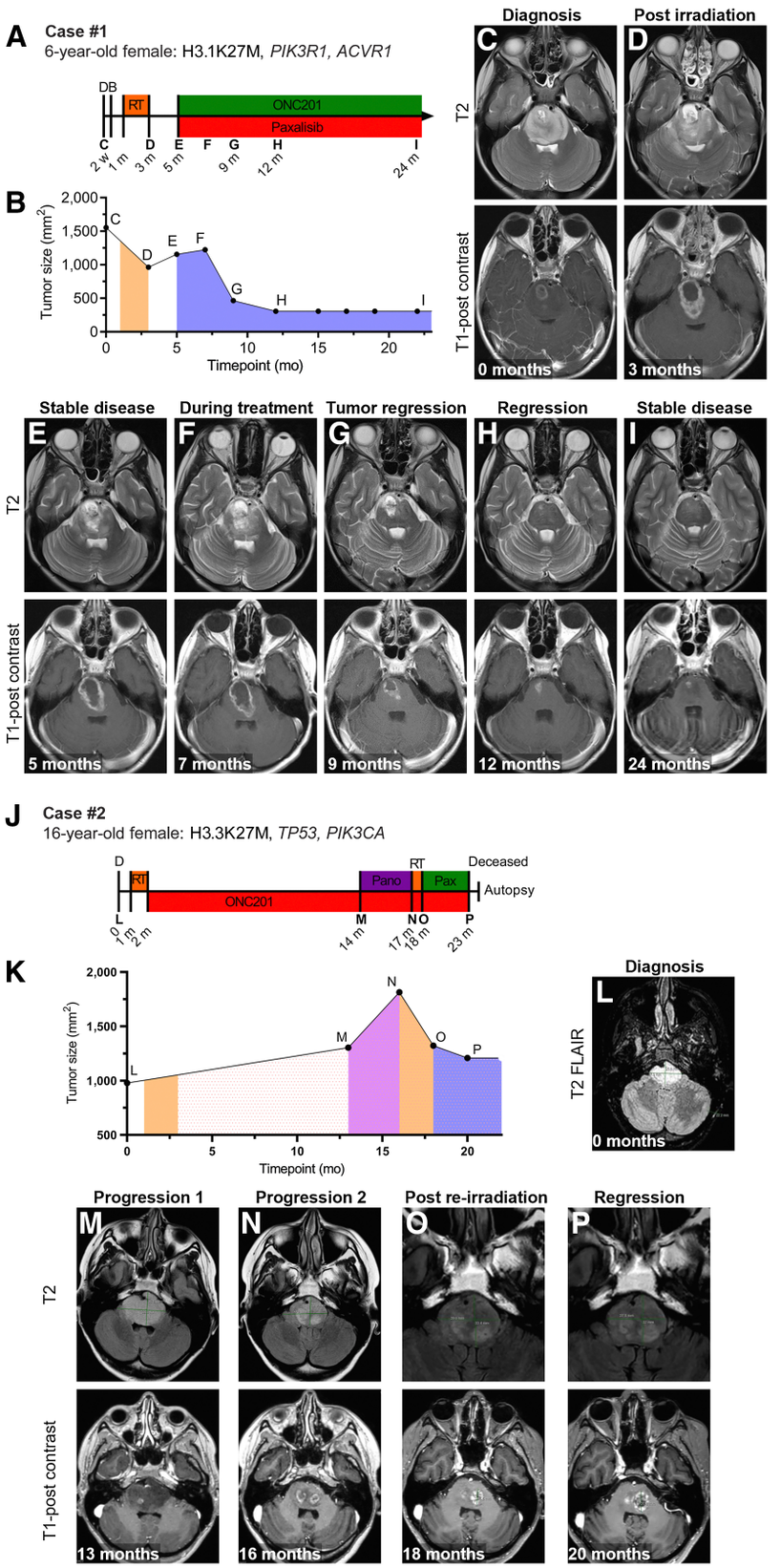

Figure 6.

ONC201 in combination with paxalisib drives tumor regression and increased survival in DIPG case studies. **A,** Six-year-old H3.1K27M, *PIK3R1, ACVR1* mutant patient with DIPG underwent biopsy soon after diagnosis and received 54 Gy radiotherapy over 30 fractions. MRI was performed six weeks after the completion of radiotherapy, and compassionate access was granted for the use of paxalisib to target *PIK3R1* mutations. Family of the patient sourced German ONC201 and started concurrently with paxalisib. **B,** Tumor size at diagnosis, following radiotherapy and throughout treatment. **C,** T2 and T1 after contrast MR axial scans at patient diagnosis, tumor area = 1,554 mm^2. **D,** Following radiotherapy, tumor area decreased by 38.1% to 962 mm^2 compared with diagnosis. **E,** MRI showed that tumor area was stable following radiotherapy = 1,156 mm^2, 20.2% progression. Following this scan, the ONC201 (15 mg/kg once a week) and paxalisib (27 mg/m^2 daily) combination was started. **F,** MRI following 8 weeks on the combination tumor area was stable (1,224 mm^2), 6% increase. **G,** Tumor regression was seen after 20 weeks on the drug combination. Tumor area = 464 mm^2; tumor reduction by 62% compared with the last scan. **H,** Most recent MRI. Tumor area = 306 mm^2; total tumor area reduction compared with diagnosis = 80%. **I,** The patient continues to remain on the combination 22 months following diagnosis. **J–P,** Sixteen-year-old H3.3K27M, *TP53, PIK3CA* mutant patient with DIPG received 54 Gy over 30 fractions. Patient enrolled in the ONC201 monotherapy trial NCT03416530 and experienced stable disease for 2 months. Following radiological and clinical progression, the patient received panobinostat (45 mg daily three times a week) with ONC201 (625 mg once a week). Further progression was seen in the subsequent MRI, where the patient then received reirradiation. The patient immediately commenced ONC201 and paxalisib, both on compassionate grounds. **K,** Tumor area measured throughout treatment. **L,** T2 and T1 after contrast MR axial scans at patient diagnosis. Tumor area = 977.8 mm^2. **M,** MRI following first progression. Tumor area = 1,303.3 mm^2. **N,** Patient received panobinostat in combination with ONC201; MRI image following the combination. Tumor area = 1,814 mm^2. Following, this patient received reirradiation and ONC201 (15 mg/kg once a week) and paxalisib (27 mg/m^2 daily) **O,** Tumor regression was seen 8 weeks after re-RT, while receiving ONC201 in combination with paxalisib. Tumor area = 1,322.6 mm^2. **P,** Tumor regression was again seen after 20 weeks on the combination; tumor area = 1,209 mm^2, 20 months after diagnosis. Patient continued to receive ONC201 and paxalisib for the next 3 months and then contracted pneumonia and passed away 24 months from diagnosis.

the child also reporting no signs of DIPG-associated clinical symptoms before the infection. NGS of post-mortem tumor tissue identified typical H3.3K27M, *TP53*, *PIK3CA* mutations (**Fig. 6J**), highlighting the potential of combined use of ONC201 and paxalisib for the treatment of DIPG at diagnosis and disease progression.

Discussion

The recent development and sharing of patient-derived models has helped to illustrate the high level of inter- and intratumoral heterogeneity of DIPG and DMG, results that highlight the need for combined therapies that target the metabolic rather than the genomic/epigenetic heterogeneity of the disease (6, 13). In this study, we have used a pharmaco–proteogenomic approach to inform a combination treatment regimen to improve response to the imipridone, ONC201, and build upon the preliminary promising efficacy of the drug for the treatment of DIPG (15, 21).

ONC201 is currently being assessed in 12 clinical trials worldwide, including in H3K27-altered gliomas (NCT03295396, NCT03416530 and NCT02525692) that reveal a preliminary survival benefit (27). ONC201 increased median OS for H3K27M brainstem tumor patients (DIPG) to 20 months ($P = 0.0002$), from the historical 11.9 months. Patients who received ONC201 outside of trials purchased by their families from a German oncologist survived 18 months, whereas those who also underwent re-irradiation survived 22 months (15, 52). Although these preliminary results are favorable, patients still succumb within 18–20 months, with some patients failing upfront treatment, indicating mechanisms of intrinsic resistance. Here, we present evidence that decreased response is influenced by PI3K/Akt signaling; prompting us to test the clinically relevant PI3K/Akt inhibitor, paxalisib (NCT03696355; refs. 28, 49), both in DIPG cell line models that were sensitive and resistant to ONC201. Combined treatment with ONC201 and paxalisib rescued the therapeutic potential of ONC201 in refractory models, independent of the availability of oxygen and independent of *TP53* status, highlighting the potential for this drug combination therapy to combat the metabolic, spatial, and genetic heterogeneity of DIPG. Commensurate with these *in vitro* discoveries, combined treatment tested in two out of three DIPG xenograft models significantly extended the survival of mice compared with monotherapies, whereas the combination had an additive effect in the other.

We show that ONC201 targets DRD2 and ClpP in DIPG models *in vitro* and xenograft models *in vivo*. DIPG models harboring *TP53* mutations show decreased sensitivity to ONC201. This is distinct from previous studies revealing ONC201 to be effective in *TP53*-mutant non-DIPG cancer models (17). Irrespective of sensitivity, ONC201 elicits potent agonism of the mitochondrial protease, ClpP, which drives mitochondrial degradation and ROS production. Previous studies showed ONC201 to be a selective antagonist of DRD2 and DRD3, causing cell death through TRAIL signaling (22). Overexpression of DRD2 has been correlated with ONC201 sensitivity (53), with antagonism shown to decrease the pro-proliferative effects of DRD2 signaling in glioblastoma, mediated, in part, by Ras/Erk, confirmed in DMG cell lines *in vitro* (15). This mode of action is in agreement with the DRD2 antagonist activity of haloperidol, an FDA approved antipsychotic, which also decreased Erk activity, analogous to the response of DIPG cells that are refractory to ONC201 (15), while having no effect on Akt. The importance of DRD2 antagonism was further highlighted following CRISPR/Cas9–mediated DRD2 KD, a strategy that proved lethal to DIPG cells *in vitro*. In several DIPG cell line models, including SU-DIPG-VI, ONC201 showed limited cytostatic effects; however, when the same cell line was implanted into the brainstem of mice, ONC201 provided a significant survival advantage compared with controls. It is plausible that these *in vivo* results reflect ONC201's role in global DRD2 antagonism rather than in the tumor alone. DIPG synthesize and secrete dopamine, a characteristic that is likely supportive of DIPG gliomagenesis (54). In glioblastoma, elevated DRD2 expression is seen in glioma-initiating cell populations, with stimulation causing neuron-like hyperpolarization exclusively driving sphere-formation and increasing tumor engraftment in PDX models (47). Here, we observe that treatment of mice with ONC201 decreased expression of TH in the prefrontal cortex suggestive of global antagonism of DRD2; however, further mechanistic insights are needed to elucidate the antitumor benefit in DMGs at this time. It is highly probable that paracrine dopamine signaling also occurs in DIPG as these cells express TH, analogous to electrochemical communications between DIPG and neurons transmitted through synapses to drive proliferation, differentiation, and survival (55). It was recently shown that DIPG patients with increased ^{18}F-DOPA uptake during MRI showed decreased sensitivity to RT ($P = 0.001$) and experienced worse outcomes independently correlating ^{18}F-DOPA uptake with OS (54). These studies highlight the potential benefit in assessing ^{18}F-DOPA during routine MRI monitoring of patients receiving ONC201 and may contribute to predicting response to ONC201.

Our studies support the findings that ClpP is an important target of ONC201 in DIPG, where agonism caused mitochondrial dysfunction (22), and *CLPP* KD abrogated ONC201's anti-DIPG effects *in vitro* (24). Regardless of sensitivity, ONC201 drives oxidative stress (following ClpP-mediated degradation of SDHA, IDH3B, CLS, COX4LI1, COX5A, and COX10; ref. 24); however, in nonsensitive cells, promotes redox activation of PI3K/Akt; however, the mechanism promoting reduced sensitivity in *TP53*-mutant lines remains unknown. Akt inactivates GSK3α/β a well-characterized mechanism of metabolic rescue driven by increased glycogen and protein synthesis to promote cell survival (49). GSK3α/β also cooperates with Kelch-like ECH-associated protein 1 (KEAP1; ref. 50) to repress the activity of the transcription factor, NRF2 (*NFE2L2)*. Yet under mitochondrial and oxidative stress, KEAP1 is degraded and NRF2 translocates to the nucleus, binding to the antioxidant response elements at gene promoters to combat oxidative stress, by promoting expression of the two-electron reductase NQO1 (38), this response could be inhibited through the combination with paxalisib to drive cell death. Here, we show that *TP53*-KO in HJSD-DIPG-007 leads to increased phosphorylation of Akt at Thr308 and Ser473, further promoting expression of NQO1 in line with this proposed mechanism of action. In addition, treatment with ONC201 increases phosphorylation of Akt at Thr308 and Ser473 further promoting expression of NQO1. It is important to note that the DIPG xenograft mouse survival benefit provided by the combination was modest, commensurate with the insidious clinical journey experienced by DIPG patients. Early clinical experience from the two cases we report using ONC201 in combination with paxalisib is promising. Both patients demonstrated resolution of clinical symptoms and radiographic tumor regression. The first patient, who demonstrated the more dramatic response and continual regression of the primary tumor extending >24 months after diagnosis, remains on the combination at the time of submission. In addition, this strategy was also used in a H3.3K27M, *TP53*, *PIK3CA* mutant DIPG patient enrolled on the phase I clinical trial (NCT03416530) testing oral ONC201 in pediatric patients with newly diagnosed DIPG, experiencing an almost complete regression of the progressive tumor to initial diagnosis size and a reversal of clinical symptoms, regression not seen following upfront RT+ONC201, although the re-RT might have

contributed to this response. Both patients tolerated the treatments well by combining treatment with dexamethasone mouthwash. The optimal dose and timing of the combination and whether these enhance the effects of standard-of-care RT either in the upfront or relapse setting remain to be determined, given that both patients also received either upfront or re-irradiation, respectively. However, in this study, we cannot explicitly rule out the contribution of paxalisib to patient response as both patients commenced ONC201 before or at the same time as paxalisib; furthermore, the contribution of paxalisib for patients harboring PI3K mutations has not yet been determined; questions that will be elucidated under clinical trial conditions. In addition, the off-target effects of paxalisib are currently unknown.

We acknowledge that ONC201 in combination with paxalisib may not be solely responsible for the almost complete resolution of the disease, particularly at advanced stages, given the modest xenograft results using immune-compromised mouse models. Indeed, H3K27M mutant DIPGs are known to reside in an immunologically cold tumor microenvironment devoid of inflammatory immune cells (7). The global loss of the H3K27me3-mediated epigenetic landscape within DIPG cells is similar to those seen in embryonic stem cells (56) characterized by little to no expression of the MHC I proteins, making these primitive cells less visible to the immune system (57). The observed change in the epigenetic landscape following ONC201 treatment and following modulation of oxidative stress may play a role in the immunogenicity of DIPG, particularly in patients with an active immune system. The partial restoration in H3K27me3 following ONC201 treatment is consistent with recent data showing that H3K27M mutations drive TCA cycle protein expression (58). Here, we show that ONC201 drives potent degradation of IDH3A/B and hence loss of mitochondrial TCA-cycle function. This, in turn, may modulate the production of epigenetic cofactors required to maintain hypomethylation of H3K27me3 (59). This highlights the emerging link between H3K27M mutations and metabolic and epigenetic plasticity (58), which may play a role in the immunogenicity of the tumor, driving an anticancer response from the immune system.

The preclinical and clinical data provided here underpin the recently commenced phase II clinical trial (NCT05009992), where we are seeking to determine whether ONC201 in combination with paxalisib is an effective regimen for treating patients with DIPG and DMG at diagnosis, after RT and at the time of progression when patients are eligible for re-irradiation. This multimodal clinical trial will assess safety of single agents in combination with upfront RT or re-irradiation for patients commencing the trial at advanced stages that we hope will form the backbone of future combination studies. We hypothesize that rationally designed combination trials, informed by rigorous preclinical data, will improve outcomes for these poor prognosis cancers. Integration of correlative studies will be critical for assessment of predictive biomarkers of response and refinement of inclusion and exclusion criteria for specific combination therapies.

Authors' Disclosures

A. Patabendige reports grants from NSW Ministry of Health, Australia and Hunter Medical Research Institute during the conduct of the study; as well as nonfinancial support from Pharmidex, UK and Flocel Inc. outside the submitted work. B. Day reports personal fees from Black Diamond Therapeutics, University of Sydney, and DC Europa outside the submitted work. J.R. Hansford reports personal fees from Bayer Australia, Boxer Capital, and Alexion Pharmaceuticals Australia outside the submitted work. R. Endersby reports other support from Cancer Council WA and Pirate Ship Foundation during the conduct of the study. N.G. Gottardo reports personal fees from Bayer, DayOne, and Eli Lily outside the submitted work. F. Alvaro reports personal fees from Norgine B.V. outside the submitted work. D.D. Eisenstat reports personal fees from Bayer Australia Ltd. outside the submitted work. M.D. Dun reports grants from Kazia Therapeutics during the conduct of the study. No disclosures were reported by the other authors.

Authors' Contributions

E.R. Jackson: Formal analysis, investigation, visualization, writing–original draft, writing–review and editing. **R.J. Duchatel:** Formal analysis, supervision, investigation, visualization, writing–original draft, writing–review and editing. **D.E. Staudt:** Formal analysis, investigation, writing–review and editing. **M.L. Persson:** Investigation. **A. Mannan:** Investigation. **S. Yadavilli:** Investigation. **S. Parackal:** Investigation. **S. Game:** Investigation. **W.C. Chong:** Investigation. **W.S.N. Jayasekara:** Investigation. **M. Le Grand:** Investigation, writing–review and editing. **P.S. Kearney:** Investigation. **A.M. Douglas:** Project administration. **I.J. Findlay:** Formal analysis, investigation. **Z.P. Germon:** Investigation. **H.P. McEwen:** Investigation. **T.S. Beitaki:** Investigation. **A. Patabendige:** Resources, writing–review and editing. **D.A. Skerrett-Byrne:** Investigation, methodology, writing–review and editing. **B. Nixon:** Methodology, writing–review and editing. **N.D. Smith:** Methodology. **B. Day:** Resources. **N. Manoharan:** Investigation, patient care. **S. Nagabushan:** Investigation, patient care. **J.R. Hansford:** Writing–review and editing. **D. Govender:** Investigation. **G.B. McCowage:** Investigation, writing–review and editing. **R. Firestein:** Writing–review and editing. **M. Howlett:** Writing–review and editing. **R. Endersby:** Writing–review and editing. **N.G. Gottardo:** Writing–review and editing. **F. Alvaro:** Investigation, writing–review and editing. **S.M. Waszak:** Investigation, writing–review and editing. **M.R. Larsen:** Methodology, writing–review and editing. **Y. Colino-Sanguino:** Writing–review and editing. **F. Valdes-Mora:** Writing–review and editing. **A. Rakotomalala:** Writing–review and editing. **S. Meignan:** Investigation, writing–review and editing. **E. Pasquier:** Resources, investigation, writing–review and editing. **N. Andre:** Writing–review and editing. **E. Hulleman:** Resources, writing–review and editing. **D.D. Eisenstat:** Writing–review and editing. **N.A. Vitanza:** Resources, writing–review and editing. **J. Nazarian:** Conceptualization, resources, supervision, writing–review and editing. **C. Koschmann:** Conceptualization, resources, supervision, writing–review and editing, patient care. **S. Mueller:** Conceptualization, resources, supervision, writing–review and editing. **J.E. Cain:** Conceptualization, resources, supervision, writing–review and editing. **M.D. Dun:** Conceptualization, resources, supervision, funding acquisition, visualization, methodology, writing–original draft, writing–review and editing.

Acknowledgments

The authors acknowledge all children and their families diagnosed with DIPG. The authors thank Profs. Michelle Monje and Angel Carcaboso for their generous gift of their DIPG cell line models. M.D. Dun is supported by a ChadTough Defeat DIPG New Investigator Grant and an NHMRC Investigator Grant—GNT1173892. The contents of the published material are solely the responsibility of the research institutions involved or individual authors and do not reflect the views of NHMRC. This project was supported by the ChadTough Defeat DIPG Foundation, RUN DIPG Ltd., Strategic Group, McDonald Jones Foundation, Vinva Foundation, PNOC Foundation, Yuvaan Tiwari Foundation, Kiriwina Investments, The Kids' Cancer Project, The DIPG Collaborative, including: The Cure Starts Now Foundation, The Cure Starts Now Australia, Brooke Healey Foundation, Wayland Villars Foundation, ChadTough Foundation, Aidan's Avengers, Austin Strong, Cure Brain Cancer, Jeffrey Thomas Hayden Foundation, Laurie's Love Foundation, Love Chloe Foundation, Musella Foundation, Pray Hope Believe, Reflections Of Grace, Storm the Heavens Fund, Aubreigh's Army, Whitley's Wishes, Ryan's Hope, Benny's World, The Isabella and Marcus Foundation, Lauren's Fight for Cure, Robert Connor Dawes Foundation, The Gold Hope Project, Julia Barbara Foundation, Lily Larue Foundation, American Childhood Cancer Organization, RUN DIPG, Gabriella's Smile Foundation, and Snapgrant.com, Charlie Teo Foundation, Little Legs Foundation, Tour de Cure, Fight on the Beaches, John Hunter Hospital Charitable Trust, Edie's Kindness Project, Liv Like A Unicorn Foundation, Maitland Cancer Appeal Committee Limited, BlackJack Pastoral Company, The Hirsch Family Funderpants, and the Hunter Medical Research Institute. Kazia Therapeutics provided funding to support personnel of M.D. Dun's laboratory. With thanks to the Isabella and Marcus Foundation, E.R. Jackson and S. Game are supported by the Miette Skiller Scholarship Fund (Josephine Dun and Elliot Gautsch Scholars, respectively), a sub-fund of the Australian Communities Foundation. E.R. Jackson is supported by an HCRA Scholarship. R.J. Duchatel is supported by a ChadTough Defeat DIPG Foundation Fellowship Grant. M. Le Grand, A. Rakotomalala, S. Meignan, and E. Pasquier received funding from "Association Wonder Augustine" and "Association Warrior Enguerrand" for their DIPG studies. M. Le Grand is supported by a postdoctoral

fellowship from the French ARC Foundation. S. Parackal is supported by a Children's Cancer Foundation/Hudson Institute Scholarship. W.C. Chong is supported by a Monash University Postgraduate Award. J.E. Cain is supported by a Victorian Cancer Agency Mid-Career Fellowship (MCRF17014). N.G. Gottardo is supported by the Perth Children's Hospital Foundation Stan Perron Chair in Pediatric Oncology and Hematology. The authors would also like to acknowledge support from the Zero Childhood Cancer Initiative, Children's Cancer Foundation, and Bailey's Day. F. Valdes-Mora is supported by the Cancer Institute NSW Fellowship CDF181218. J.R. Hansford is supported through grants from the McClurg and Hospital Research Foundations. The clinical trial is supported by Mithil Prasad Foundation, ChadTough Defeat DIPG Foundation, and Storm the Heavens, the last also supporting S. Meignan. Proteomics was facilitated by N.D. Smith from The Analytical and Biomolecular Research Facility and The Academic and Research Computing Support (ARCS) team, within IT Services at the University of Newcastle, who provided high-performance computing (HPC) infrastructure for bioinformatics analyses. Histology services were provided by Cassandra Griffin, Fiona Richards, Megan Clarke, and Kaylee O'Brien from the HMRI Core Histology Facility. IHC optimization and staining services were provided by The University of Newcastle's "NSW Regional Biospecimen and Research Services," with support from NSW Health Pathology.

The publication costs of this article were defrayed in part by the payment of publication fees. Therefore, and solely to indicate this fact, this article is hereby marked "advertisement" in accordance with 18 USC section 1734.

Note

Supplementary data for this article are available at Cancer Research Online (http://cancerres.aacrjournals.org/).

Received March 22, 2023; revised April 26, 2023; accepted May 3, 2023; published first May 5, 2023.

References

1. Ostrom QT, Gittleman H, Liao P, Vecchione-Koval T, Wolinsky Y, Kruchko C, et al. CBTRUS statistical report: primary brain and other central nervous system tumors diagnosed in the United States in 2010–2014. Neuro Oncol 2017;19:v1–v88.
2. Warren K. Diffuse intrinsic pontine glioma: poised for progress. Front Oncol 2012;2:205.
3. Hoffman LM, Veldhuijzen van Zanten SEM, Colditz N, Baugh J, Chaney B, Hoffmann M, et al. Clinical, radiologic, pathologic, and molecular characteristics of long-term survivors of diffuse intrinsic pontine glioma (DIPG): a collaborative report from the international and European society for pediatric oncology DIPG registries. J Clin Oncol 2018;36:1963–72.
4. Sulman EP, Eisenstat DD. World cancer day 2021—perspectives in pediatric and adult neuro-oncology. Front Oncol 2021;11:659800.
5. Pincus DW, Richter EO, Yachnis AT, Bennett J, Bhatti MT, Smith A. Brainstem stereotactic biopsy sampling in children. J Neurosurg 2006;104:108–14.
6. Findlay IJ, De Iuliis GN, Duchatel RJ, Jackson ER, Vitanza NA, Cain JE, et al. Pharmaco-proteogenomic profiling of pediatric diffuse midline glioma to inform future treatment strategies. Oncogene 2022;41:461–75.
7. Persson ML, Douglas AM, Alvaro F, Faridi P, Larsen MR, Alonso MM, et al. The intrinsic and microenvironmental features of diffuse midline glioma: implications for the development of effective immunotherapeutic treatment strategies. Neuro Oncol 2022;24:1408–22.
8. Khuong-Quang DA, Buczkowicz P, Rakopoulos P, Liu XY, Fontebasso AM, Bouffet E, et al. K27M mutation in histone H3.3 defines clinically and biologically distinct subgroups of pediatric diffuse intrinsic pontine gliomas. Acta Neuropathol 2012;124:439–47.
9. Schwartzentruber J, Korshunov A, Liu XY, Jones DT, Pfaff E, Jacob K, et al. Driver mutations in histone H3.3 and chromatin remodelling genes in paediatric glioblastoma. Nature 2012;482:226–31.
10. Wu G, Broniscer A, McEachron TA, Lu C, Paugh BS, Becksfort J, et al. Somatic histone H3 alterations in pediatric diffuse intrinsic pontine gliomas and non-brainstem glioblastomas. Nat Genet 2012;44:251–3.
11. Antin C, Tauziede-Espariat A, Debily MA, Castel D, Grill J, Pages M, et al. EZHIP is a specific diagnostic biomarker for posterior fossa ependymomas, group PFA and diffuse midline gliomas H3-WT with EZHIP overexpression. Acta Neuropathol Commun 2020;8:183.
12. Chan KM, Fang D, Gan H, Hashizume R, Yu C, Schroeder M, et al. The histone H3.3K27M mutation in pediatric glioma reprograms H3K27 methylation and gene expression. Genes Dev 2013;27:985–90.
13. Mackay A, Burford A, Carvalho D, Izquierdo E, Fazal-Salom J, Taylor KR, et al. Integrated molecular meta-analysis of 1,000 pediatric high-grade and diffuse intrinsic pontine glioma. Cancer Cell 2017;32:520–37.
14. Duchatel RJ, Jackson ER, Alvaro F, Nixon B, Hondermarck H, Dun MD. Signal transduction in diffuse intrinsic pontine glioma. Proteomics 2019;19:e1800479.
15. Duchatel RJ, Mannan A, Woldu AS, Hawtrey T, Hindley PA, Douglas AM, et al. Preclinical and clinical evaluation of German-sourced ONC201 for the treatment of H3K27M mutant diffuse intrinsic pontine glioma. Neurooncol Adv 2021;3:vdab169.
16. Arrillaga-Romany I, Kurz S, Tarapore R, Lu G, Sumrall A, Butowski N, et al. Clinical efficacy of ONC201 in recurrent H3 K27M-mutant diffuse midline glioma patients. Neuro Oncol 2021;23:vi230-vi.
17. Ishizawa J, Kojima K, Chachad D, Ruvolo P, Ruvolo V, Jacamo RO, et al. ATF4 induction through an atypical integrated stress response to ONC201 triggers p53-independent apoptosis in hematological malignancies. Sci Signal 2016;9:ra17.
18. Wagner J, Kline CL, Zhou L, Khazak V, El-Deiry WS. Anti-tumor effects of ONC201 in combination with VEGF-inhibitors significantly impacts colorectal cancer growth and survival in vivo through complementary non-overlapping mechanisms. J Exp Clin Cancer Res 2018;37:11.
19. Greer YE, Porat-Shliom N, Nagashima K, Stuelten C, Crooks D, Koparde VN, et al. ONC201 kills breast cancer cells *in vitro* by targeting mitochondria. Oncotarget 2018;9:18454–79.
20. Fang Z, Wang J, Clark LH, Sun W, Yin Y, Kong W, et al. ONC201 demonstrates anti-tumorigenic and anti-metastatic activity in uterine serous carcinoma *in vitro*. Am J Cancer Res 2018;8:1551–63.
21. Arrillaga-Romany I, Chi AS, Allen JE, Oster W, Wen PY, Batchelor TT. A phase 2 study of the first imipridone ONC201, a selective DRD2 antagonist for oncology, administered every three weeks in recurrent glioblastoma. Oncotarget 2017;8:79298–304.
22. Allen JE, Krigsfeld G, Mayes PA, Patel L, Dicker DT, Patel AS, et al. Dual inactivation of Akt and ERK by TIC10 signals Foxo3a nuclear translocation, TRAIL gene induction, and potent antitumor effects. Sci Transl Med 2013;5:171ra17.
23. Ishizawa J, Zarabi SF, Davis RE, Halgas O, Nii T, Jitkova Y, et al. Mitochondrial ClpP-mediated proteolysis induces selective cancer cell lethality. Cancer Cell 2019;35:721–37.
24. Madhukar NS, Khade PK, Huang L, Gayvert K, Galletti G, Stogniew M, et al. A bayesian machine learning approach for drug target identification using diverse data types. Nat Commun 2019;10:5221.
25. Przystal JM, Cianciolo Cosentino C, Yadavilli S, Zhang J, Laternser S, Bonner ER, et al. Imipridones affect tumor bioenergetics and promote cell lineage differentiation in diffuse midline gliomas. Neuro Oncol 2022;24:1438–51.
26. Pruss M, Dwucet A, Tanriover M, Hlavac M, Kast RE, Debatin KM, et al. Dual metabolic reprogramming by ONC201/TIC10 and 2-Deoxyglucose induces energy depletion and synergistic anti-cancer activity in glioblastoma. Br J Cancer 2020;122:1146–57.
27. Kawakibi AR, Tarapore RS, Gardner S, Chi A, Kurz S, Wen PY, et al. Hgg-18. clinical efficacy of Onc201 in thalamic H3 K27m-mutant glioma. Neuro-oncol 2020;22:iii347–iii.
28. Duchatel R, Jackson E, Patabendige A, Cain J, Tsoli M, Monje M, et al. DIPG-03. targeting PI3K using the blood brain barrier penetrable inhibitor, GDC-0084, for the treatment of diffuse intrinsic pontine glioma (DIPG). Neuro-oncol 2019;21:ii68–ii.
29. Wen PY, Cloughesy TF, Olivero AG, Morrissey KM, Wilson TR, Lu X, et al. First-in-human Phase I study to evaluate the brain-penetrant PI3K/mTOR inhibitor GDC-0084 in patients with progressive or recurrent high-grade glioma. Clin Cancer Res 2020;26:1820–8.

30. Hutcheon K, McLaughlin EA, Stanger SJ, Bernstein IR, Dun MD, Eamens AL, et al. Analysis of the small non–protein-coding RNA profile of mouse spermatozoa reveals specific enrichment of piRNAs within mature spermatozoa. RNA Biol 2017;14:1776–90.
31. Khan A, Gamble LD, Upton DH, Ung C, Yu DMT, Ehteda A, et al. Dual targeting of polyamine synthesis and uptake in diffuse intrinsic pontine gliomas. Nat Commun 2021;12:971.
32. Dun MD, Anderson AL, Bromfield EG, Asquith KL, Emmett B, McLaughlin EA, et al. Investigation of the expression and functional significance of the novel mouse sperm protein, a disintegrin and metalloprotease with thrombospondin Type 1 motifs number 10 (ADAMTS10). Int J Androl 2012;35:572–89.
33. Degryse S, de Bock CE, Demeyer S, Govaerts I, Bornschein S, Verbeke D, et al. Mutant JAK3 phosphoproteomic profiling predicts synergism between JAK3 inhibitors and MEK/BCL2 inhibitors for the treatment of T-cell acute lymphoblastic leukemia. Leukemia 2018;32:788–800.
34. Aoki Y, Hashizume R, Ozawa T, Banerjee A, Prados M, James CD, et al. An experimental xenograft mouse model of diffuse pontine glioma designed for therapeutic testing. J Neurooncol 2012;108:29–35.
35. Ozawa T, James CD. Establishing intracranial brain tumor xenografts with subsequent analysis of tumor growth and response to therapy using bioluminescence imaging. J Vis Exp 2010:1986. doi: 10.3791/1986.
36. Perez-Riverol Y, Bai J, Bandla C, Garcia-Seisdedos D, Hewapathirana S, Kamatchinathan S, et al. The PRIDE database resources in 2022: a hub for mass spectrometry-based proteomics evidences. Nucleic Acids Res 2022;50:D543–D52.
37. Arrillaga-Romany I, Odia Y, Prabhu VV, Tarapore RS, Merdinger K, Stogniew M, et al. Biological activity of weekly ONC201 in adult recurrent glioblastoma patients. Neuro Oncol 2020;22:94–102.
38. Rakotomalala A, Bailleul Q, Savary C, Arcicasa M, Hamadou M, Huchede P, et al. H3.3K27M mutation controls cell growth and resistance to therapies in pediatric glioma cell lines. Cancers 2021;13:5551.
39. Bax DA, Little SE, Gaspar N, Perryman L, Marshall L, Viana-Pereira M, et al. Molecular and phenotypic characterisation of paediatric glioma cell lines as models for preclinical drug development. PLoS ONE 2009;4:e5209.
40. Xu C, Liu H, Pirozzi CJ, Chen LH, Greer PK, Diplas BH, et al. TP53 wild-type/PPM1D mutant diffuse intrinsic pontine gliomas are sensitive to a MDM2 antagonist. Acta Neuropathol Commun 2021;9:178.
41. Zhang M, Zhuang G, Sun X, Shen Y, Wang W, Li Q, et al. TP53 mutation-mediated genomic instability induces the evolution of chemoresistance and recurrence in epithelial ovarian cancer. Diagn Pathol 2017;12:16.
42. McLeod C, Gout AM, Zhou X, Thrasher A, Rahbarinia D, Brady SW, et al. St. Jude Cloud: a pediatric cancer genomic data-sharing ecosystem. Cancer Discov 2021;11:1082–99.
43. Martinez-Reyes I, Chandel NS. Mitochondrial TCA cycle metabolites control physiology and disease. Nat Commun 2020;11:102.
44. Li J, Zhu S, Kozono D, Ng K, Futalan D, Shen Y, et al. Genome-wide shRNA screen revealed integrated mitogenic signaling between dopamine receptor D2 (DRD2) and epidermal growth factor receptor (EGFR) in glioblastoma. Oncotarget 2014;5:882–93.
45. Ali AK, Nandagopal N, Lee SH. IL15–PI3K–AKT–mTOR: a critical pathway in the life journey of natural killer cells. Front Immunol 2015;6:355.
46. Pallmann N, Livgard M, Tesikova M, Zeynep Nenseth H, Akkus E, Sikkeland J, et al. Regulation of the unfolded protein response through ATF4 and FAM129A in prostate cancer. Oncogene 2019;38:6301–18.
47. Tonelli C, Chio IIC, Tuveson DA. Transcriptional regulation by Nrf2. Antioxid Redox Signal 2018;29:1727–45.
48. Drainas AP, Lambuta RA, Ivanova I, Sercin O, Sarropoulos I, Smith ML, et al. Genome-wide screens implicate loss of cullin ring ligase 3 in persistent proliferation and genome instability in TP53-deficient cells. Cell Rep 2020;31:107465.
49. He C, Xu K, Zhu X, Dunphy PS, Gudenas B, Lin W, et al. Patient-derived models recapitulate heterogeneity of molecular signatures and drug response in pediatric high-grade glioma. Nat Commun 2021;12:4089.
50. Rose WC, Wild R. Therapeutic synergy of oral taxane BMS-275183 and cetuximab versus human tumor xenografts. Clin Cancer Res 2004;10:7413–7.
51. Mueller S, Hashizume R, Yang X, Kolkowitz I, Olow AK, Phillips J, et al. Targeting wee1 for the treatment of pediatric high-grade gliomas. Neuro Oncol 2014;16:352–60.
52. Andre N, Buyens G, Bouffet E, Walker D, Dun MD. Access to new drugs in paediatric oncology: can we learn from the ongoing ONC201 saga? Lancet Oncol 2023;24:209–12.
53. Kline CLB, Ralff MD, Lulla AR, Wagner JM, Abbosh PH, Dicker DT, et al. Role of dopamine receptors in the anticancer activity of ONC201. Neoplasia 2018;20:80–91.
54. Morana G, Tortora D, Bottoni G, Puntoni M, Piatelli G, Garibotto F, et al. Correlation of multimodal (18)F-DOPA PET and conventional MRI with treatment response and survival in children with diffuse intrinsic pontine gliomas. Theranostics 2020;10:11881–91.
55. Venkatesh HS, Morishita W, Geraghty AC, Silverbush D, Gillespie SM, Arzt M, et al. Electrical and synaptic integration of glioma into neural circuits. Nature 2019;573:539–45.
56. Harutyunyan AS, Krug B, Chen H, Papillon-Cavanagh S, Zeinieh M, De Jay N, et al. H3K27M induces defective chromatin spread of PRC2-mediated repressive H3K27me2/me3 and is essential for glioma tumorigenesis. Nat Commun 2019;10:1262.
57. Drukker M, Katz G, Urbach A, Schuldiner M, Markel G, Itskovitz-Eldor J, et al. Characterization of the expression of MHC proteins in human embryonic stem cells. Proc Natl Acad Sci U S A 2002;99:9864–9.
58. Chung C, Sweha SR, Pratt D, Tamrazi B, Panwalkar P, Banda A, et al. Integrated metabolic and epigenomic reprograming by H3K27M mutations in diffuse intrinsic pontine gliomas. Cancer Cell 2020;38:334–49.
59. Ceccarelli M, Barthel FP, Malta TM, Sabedot TS, Salama SR, Murray BA, et al. Molecular profiling reveals biologically discrete subsets and pathways of progression in diffuse glioma. Cell 2016;164:550–63.